Boulder abundances and size-frequency distributions on Oxia Planum-Mars: Scientific implications for the 2020 ESA ExoMars rover

Maurizio Pajola[1], Sandro Rossato[2], Emanuele Baratti[3], Riccardo Pozzobon[2], Cathy Quantin[4], John Carter[5], Patrick Thollot[4]
1 NASA Ames Research Center, Moffett Field, CA 94035, USA.
2 Geosciences Department, University of Padova, Padova, Italy.
3 School of Engineering and Architecture, Department DICAM, University of Bologna, Bologna, Italy.
4 Laboratoire de Géologie de Lyon Terre, Planètes, Environnement (CNRS-ENSLyon-Université), Lyon1, France.
5 Institut d'Astrophysique Spatial, Université Paris 11-Orsay, France.

Abstract--

This paper presents the abundances and the size-frequency distributions (SFD) of boulders identified on a sector of the **prime** landing site for the ExoMars 2020 rover, in Oxia Planum region. By means of a HiRISE image, boulders ≥1.75 m **across** have been identified and subdivided according to the two main Oxia Planum geological units: the Noachian clay-rich formation (Nc), and the Amazonian volcanic deposit (Av).

The spatial density of boulders ≥1.75 m over the entire study area is $6.75\times10^{-4}/m^2$, with a size-frequency that **is best fit both with power-law and exponential-law curves with indices of -4.9+0.1/-0.2 and -1.29 +0.04/-0.06 respectively. Significant differences were found by analysing separately the Av and Nc geological units. The data collected in the Av unit are well-fitted with a power-law curve with an index equal to -4.8 +/-0.2 and with an exponential-law curve with an index of -1.24 +0.05,-0.06, whilst in the Nc unit such indices are -5.5 +0.3/-0.4 and -1.70 +0.09/-0.12 (power-law and exponential-law curve, respectively).**

The spatial density of boulders in the Av unit is 7.0 times **larger** than in the Nc one. This may be due primarily to the distinct mechanical properties of the two units that may result in a different production rate or preservation of the boulders. Secondly, the Av unit overlies the Nc unit, possibly resulting in more impacts and/or different weathering processes throughout the ages.

This study provides a quantitative evaluation of the abundances **of boulders** ≥ 1.75 m **across** on Oxia Planum: it is therefore a reference for the ExoMars 2020 mission, both during the landing phase and the rover traverse to specific areas of interest. The landing **ellipse** presents much higher **abundances** of boulders ≥ 1.75 m than all previous Martian rover landing areas. This is particularly evident when the rougher Av unit is taken into account. Contrarily, the Nc unit shows a much more comparable value, but still slightly higher, to the Mars Pathfinder landing site. We provide illustrative navigating scenarios for both the Nc and the Av units as well.

1.0 Introduction

More than 50 years ago, in 1965, the first unearthly boulders were revealed on the lunar surface thanks to the Ranger probe photographs (Kuiper et al., 1965). Afterwards, in 1977, both Viking spacecraft photographed Martian boulders (**Mutch et al., 1977**), suggesting that they might be ubiquitous on solid planetary surfaces. From that moment on, both the increasing number of different imaged bodies, as well as the increasing dataset resolutions, led to the possibility **of studying the size-frequency distribution (SFD)** of boulders present on the surface of a Solar system body.

Today, boulder SFD analysis is a widely accepted and useful tool to test and investigate the geomorphological processes that occurred, or are still occurring, on a planetary surface (e.g., McGetchin et al., 1973; Garvin et al. 1981; Craddock et al. 2000; Ward et al. 2005; Grant et al. 2006; Yingst et al. 2007, Golombeck et al. 2008, Yingst et al. 2010). This approach is not only used for planets, but there is also a vast literature documenting the SFD of boulders due to impact cratering on the Martian satellites Phobos and Deimos (e.g., Lee et al., 1986**),** on asteroids like 243 Ida, 433 Eros, 25143 Itokawa and 21 Lutetia (Geissler et al., 1996,Thomas et al., 2001,Michikami et al., 2008; Mazrouei et al. 2014, Kueppers et al., 2012), on the Moon (Bart and Melosh, 2010), and, more recently, on cometary nuclei, e.g. 67P/Churyumov-Gerasimenko and 103P/Hartley 2 (Pajola et al., 2015, Pajola et al., 2016a).

For the specific case of Mars, multiple studies have related the derived SFD of boulders not only to impact cratering (e.g., Melosh 1989), but also to erosive and depositional phenomena (e.g., Christensen P. R. 1986), as well as to aeolian processes (e.g., Hebrard et al. 2012). In addition, thanks to the availability of in situ data obtained by landers and rovers, it has been demonstrated that boulders are fundamental science targets that contain information both on the **morphological** processes on Mars, as presented **at** the Viking 1 (Chryse Planitia) and Viking 2 (Utopia Planitia) landing **sites** (Mutch et al., 1976a,b), and on the mineralogy and geochemistry of its surface, as presented **at the** Pathfinder landing site (Morris et al., 2000), **at** Gusev crater by the rover Spirit (Hamilton & Ruff (2012)), **at** Meridiani Planum by Opportunity (Squyres et al., 2006), and **at** Gale crater by the Curiosity rover (Stolper et al., 2013).

In this context, the boulder abundances and the corresponding SFD **are** strictly related to the safety of a landing probe as well as to the roving (Golombek and Rapp, 1997; Golombek et al., 2003a,b, 2008, 2012, Pajola 2015b,c). Indeed, this aspect is one of the pivotal engineering **constraints** in a landing site selection process (see, e.g., the call for Landing Site selection for the ExoMars rover: http://exploration.esa.int/mars/53458-exomars-2018-landing-site-selection-users-manual/ Reference: EXM-SCI-LSS-ESA/IKI-003).

To date, analysis of the boulders on the surface of Mars **has used** the images obtained by the High Resolution Imaging Science Experiment, HiRISE, which achieves a resolution of 0.25 m/pixel (McEwen et al., 2007). The identification of the boulders can be made both manually or by using automated algorithms (Golombek et al., 2008). In the first case, the analysis is particularly time consuming, therefore the investigated area is often smaller than the one that can be considered when an automatic routine is used. On the contrary, the automatic detection generally allows the collection of a large amount of data, but a manual validation is always required in order to avoid biased analyses (e.g. Cheng et al., 2001; Huertas, et al., 2006; Matthies et al., 2007, Golombek et al., 2008, Aboudan et al., 2014).

In this paper an analysis of the boulder abundances and their SFD is presented. The study area is located inside the landing ellipse of the primary candidate for the ExoMars 2020 mission, namely "Oxia Planum" (http://exploration.esa.int/mars/56686-landing-site-recommended-for-exomars-2018/). This area lies between the southern highlands of Arabia Terra and the northern plains of Chryse Planitia (Fig. 1). The analysis focuses on boulders that have been manually identified in a HiRISE image and then grouped on the basis of homogeneous geological units. Their SFD, as well as the densities per m^2 and the corresponding power-law and exponential-law indices are presented **(in a log-log plot where the y axis is the cumulative number of boulder per m^2 and the x axis is boulder size expressed in meters, the power-law index is the slope value of the regression line that fits the SFD of the boulders, while the exponential-law indices are the multiplying factor and the exponent of the exponential curve fitting the data). Finally, the** implications **for** safety and risks as well as the navigability of this area for the ExoMars 2020 mission are discussed.

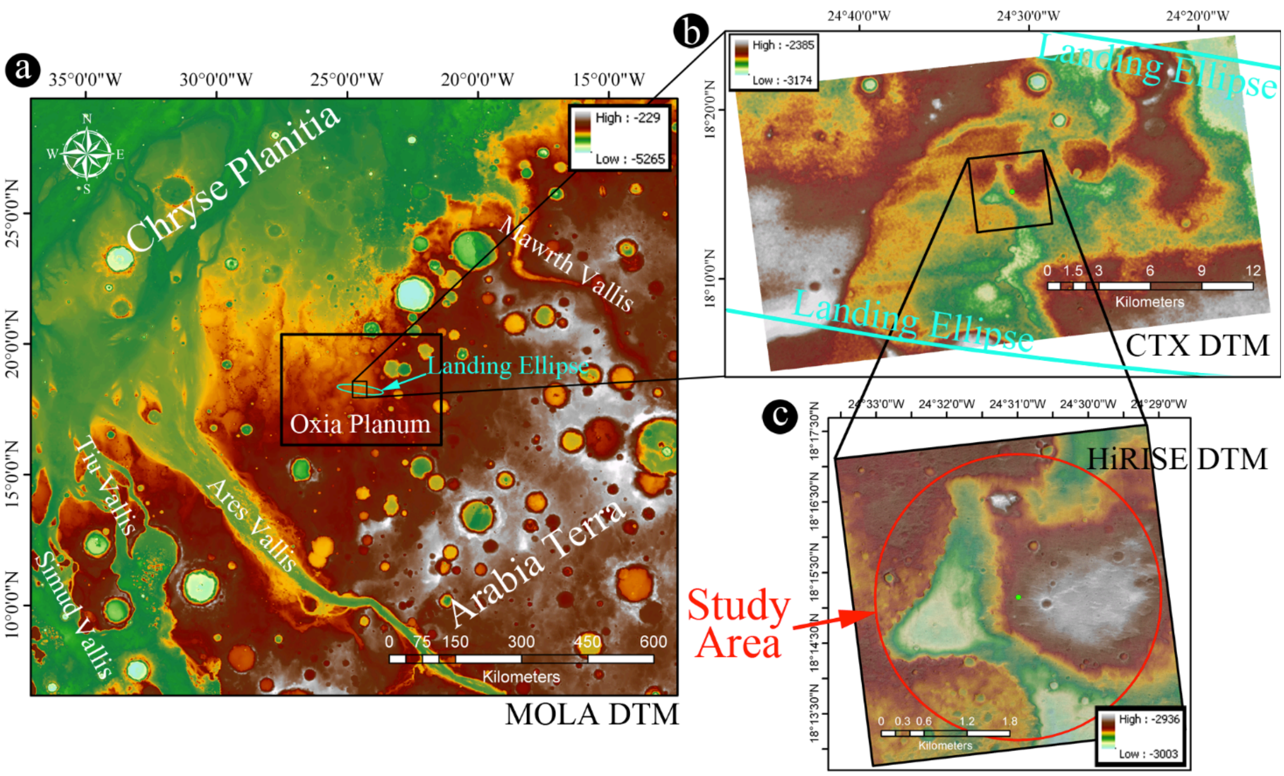

Fig. 1. (a) MOLA context map showing the location of the Oxia Planum region (black rectangle) **and the landing ellipse for the ExoMars 2020 mission. The primary landing ellipse (light blue) is 104 × 19 km wide, is oriented with an azimuth angle of 97°30' and its center is located at -24°30'59''E and 18°15'9"N.** (b) CTX DTM located at the center of the ExoMars landing ellipse **(light blue)** with a spatial scale of **22 m/pixel**. (c) HiRISE DTM covering the center of the Oxia Planum proposed landing ellipse. The spatial scale is **1 m/pixel**. **The red circle indicated by a red arrow is the study area** where the boulder identification was performed. In (b) and (c) the green dot represents the center of the proposed landing ellipse.

2.0 Material and Methods

2.1 Imaging

The analysis of the Oxia Planum surface was performed by importing into the ArcGIS environment the HiRISE PSP_009880_1985_RED equirectangular map-projected image downloaded from the HiRISE image repository (http://www.uahirise.org). This image covers the center of the landing ellipse of the primary candidate for the ExoMars 2020 mission (Fig. 1, Quantin et al., 2015) with a swath that is 18.6 km long and 6.1 km wide; it is centered at 18.2°N and -24.5°E and was taken during MRO orbit #9880 with a phase angle of 55.77°, an emission angle of 7.8°, and a solar incidence angle of 48°, with the Sun 42° above the horizon. This image was taken at a distance of 285.3 km from the target surface, with an original scale range of 28.5 cm/pixel (with 1 × 1 binning); therefore, as stated in the HiRISE repository site for this image, objects larger than **85** cm across are here resolved. The resulting map projected scale is 0.25 m/pixel.

2.2 High-resolution stereo DTM generation and validation

Digital Terrain Models (DTMs) of the study area were produced in order to **allow** detailed characterization of the differences in elevation **within** our study area. In addition, such DTMs were used to investigate the different geological units of the area as well as to prepare the slope map of the area.
We chose a multi-scale approach in order to have an overall estimate of the Oxia region topography and a more detailed one **at** the center of the Oxia Planum landing site. Since **the resolution of**

MOLA MEGDR topography (~463 m, Smith et al., 2001) **is insufficient for our purposes**, we used stereo DTMs derived both from CTX and HiRISE images. For this purpose, we selected a pair of the best overlapping CTX (~6 m/pixel, see Table 1) images and the single available HiRISE stereo pair (PSP_009735_1985_RED, PSP_009880_1985_RED).

All DTMs were produced and validated with **the** HRSC DTM (100 m/pixel) and **the** MOLA spheroid **through the** Ames Stereo Pipeline software (Moratto et al., 2010). All images were pre-processed with ISIS3 software (Integrated Software for Imagers and Spectrometers, Torson and Becker, 1997). CTX raw images underwent pre-processing involving attachment of SPICE kernels for camera pointing, radiometric calibration and destriping and projection. In addition, the HiRISE raw EDR data (experiment data records) were mosaicked, calibrated and de-jittered.

The most important step before stereo matching was the bundle adjustment, required to obtain a validated DTM suitable for scientific analysis. This technique corrects the biases potentially affecting the DTM generated by erroneous pointing during acquisition of images that could result in altered surface features and inconsistency of the slopes. Bundle adjustment iteratively adjusts the position of the observer until the shift of the retro-projection of the pixels constituting the surface is minimized (Moratto et al., 2010).

After the generation of the 3D point cloud created by the stereo matching, the *pc_align* tool was used to match the obtained point clouds with a reference-fixed one, in our case a HRSC DTM (Table 1). This tool aligns and minimizes the shift in height of the obtained point cloud and its possible displacement. In addition, it deletes the points that are too far from the reference point cloud and are not properly matching, degrading the overall accuracy (Moratto et al., 2010). We adopted the H3059_0000_DT4.IMG HRSC DT4 as a reference for the alignment, because of its height calibration on the Martian spheroid. The point cloud was then used to create a DTM according to the techniques described in Moratto et al., (2010), using a 4x post spacing of the input image ground scale for CTX (5.6 m/pixel) and HiRISE (0.25 cm/pixel), resulting in an improved matching reliability (Moratto et al., 2010). We obtained DTMs of 22 m and 1 m **post-spacing** for **CTX and HiRISE respectively. The DTMs that were produced have an absolute height referred to the MOLA geoid (Fig. 1) and the vertical precision is estimated at ~4 m for CTX and ~0.4 m for HiRISE computed with the PILOT stereo matching tool (Bailen et al., 2015; Becker et al., 2015). The original HiRISE orthoimage we used is PSP_009880_1985_RED and, in this case, the pixel resolution was kept at 0.285 m/pixel to preserve the original information at its best, while the CTX stereo pair bears a pixel resolution of 5.65 m/pixel (resolving objects ~17 m across) then resampled at 6 m/pixel.** Such topographic information, coupled with other derived maps (e.g. the slope map, obtained with ArcGIS 3D analyst function), was **used** in our analysis.

Table 1: The HiRISE and CTX stereo pairs used in this work to produce the high-resolution DTMs. The HRSC DT4 used for their alignment is also included.

Instrument	Stereo couple product IDs	Pixel Scale	Phase Angle	Convergence Angle
HiRISE	PSP_009735_1985_RED PSP_009880_1985_RED	0.285 m/pixel 0.285 m/pixel	55.8° 41.2°	16.2°
CTX	P22_009735_1977_XN_17N024W B01_009880_1977_XN_17N024W	5.64 m/pixel 5.65 m/pixel	41.4° 55.9°	16.3°
HRSC DTM	H3059_0000_DT4.IMG	-	-	-

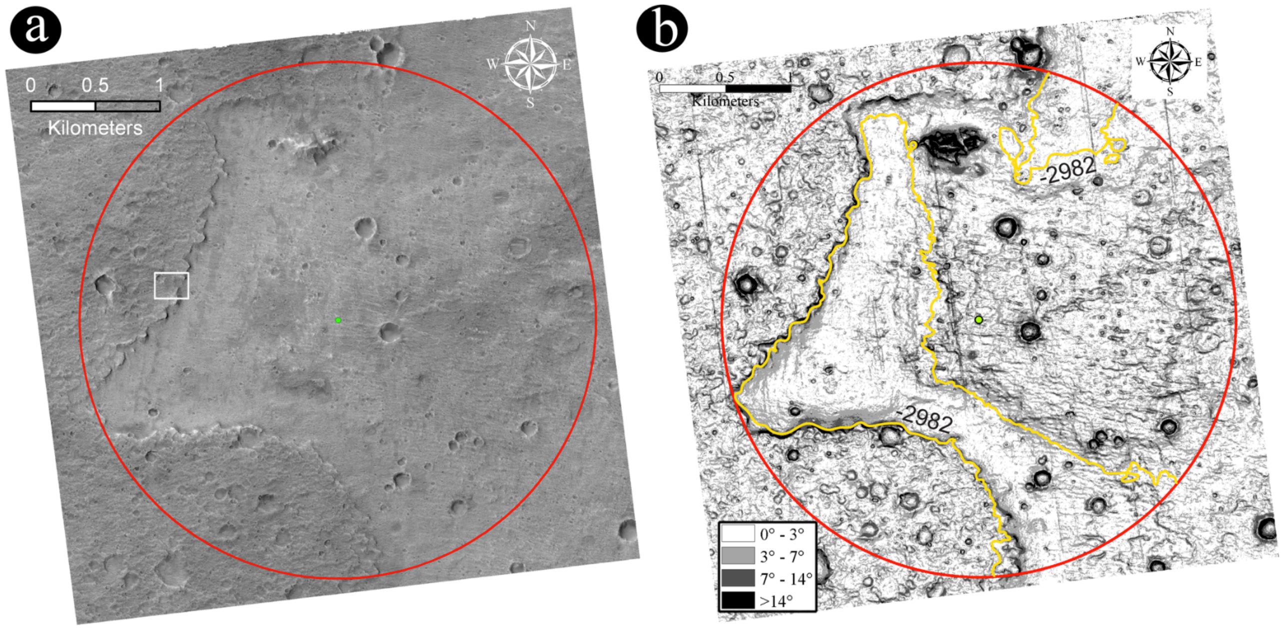

Fig. 2: (a) **Orthorectified HiRISE** image (PSP_009880_1985_RED) showing the Oxia Planum study area with a spatial scale of 0.285 m/pixel. The white rectangle shows the location of Fig. 3. (b) Slope map computed in degrees (Burrough and McDonell, 1998) and derived using the HiRISE DTM presented in Fig. 1c that covers the same surface of (a). The slope map is calculated at 1 m length scale. In both images the green dot **represents** the center of the proposed landing ellipse and the red circle corresponds to the boulder counting area (as for Fig. 1). **The yellow line in b shows the -2982 m elevation referred to in the text.**

2.3 Boulder identification

Our primary intent is to evaluate the average boulder abundance and associated SFD in a sector of the ExoMars 2020 **prime** landing ellipse. To do so, we chose a circular study area (2 km radius - red circle in Fig. 1c and Fig. 2) centered on the landing ellipse center, and we manually identified the boulders inside it. Moreover, this area, 12.57 km^2, has been selected because it includes the two main geological units which have been mapped in the Oxia Planum region (Quantin et al., 2015) (see Section 3.0 for a detailed description), thus allowing **for the possibility of obtaining** useful insights into their evolution.

A "boulder" is defined as “a positive relief detectable with the presence of an elongated shadow (if the phase angle is greater than 0°), and appearing detached from the ground where it stands” (Pajola et al., 2015, 2016d). Following the official USGS size terms after Wentworth (1922), “boulders” have diameters >0.25 m, whereas “cobbles” range between 0.25 and 0.064 m and “pebbles” sizes range between 0.064 and 0.002 m. **Since the rocks we identify in this analysis are all bigger than 1.75 m, i.e. much more than the official USGS 0.25 m limit, we call them “boulders”. We recall that with the HiRISE images we are using, objects larger than 85 cm across are resolved, as stated in the HiRISE repository site for this image.** Scarps and bedrock ledges are characterized by elongated and aligned shapes that cast shadows on the surface as well but with contiguous, if not uninterrupted shapes that are different to **those of** the commonly isolated **boulders** (see white ellipses in Fig. 3). Hills and mounds, on the contrary, present isolated shadows similar to **those of** the boulders, but such features are morphologically emerging from the ground itself **(as also visible and measurable in the related DTM and orthoimage)** instead of appearing detached from the ground (white boxes in Fig. 3). Following these guidelines, in this work we can define all the identified features as “boulders”.

Following Golombeck et al. (2003a, 2008), the detection of the boulders was based on the presence of their associated shadows. In particular, the boulders are approximated by circles

centered at the estimated boulder position based on the shadow (see Fig. 3a and 3b). Their diameter extends up to the terminator and partially overlap the shadows. The location of each boulder, its diameter, and area are recorded. Fig. 3c and d shows the results of our boulder identification methodology applied on a test area. We used ArcGis 10.4 software for the identification and mapping.

We here underline that despite the common use of a circular shape for the considered boulders, we do not mean that the mechanisms we propose for the boulder formation and evolution have to be equant. We are aware that boulders can have elongated shapes, but we are focusing on their maximum dimension distribution, as done in several other works not involving the boulders' morphometry, e.g. Golombek et al., 2003; Michikami et al., 2008, Kueppers et al., 2012. By knowing the pixel scale of the image, the boulders' diameters and the corresponding areas where they are located were then derived. The resolution of the HiRISE images allows the detection of features down to 0.75 m in diameter (3 pixels sampling rule, Nyquist 1928**). Nonetheless,** it is not uncommon that more than 3 pixels, e.g. 4-7 pixels, are considered as **a** lower boundary to provide a meaningful size-frequency statistic (Mazrouei et al., 2014; Pajola et al., 2015). Indeed, in this way, the likelihood of boulder misidentifications is minimized. Moreover, according to previous studies (e.g. Golombek et al., 2008), the smallest measurable boulder using shadows in HiRISE images is typically ~1.5 m across.

The HiRISE image we used was **obtained at** a phase angle of ~56°, hence the presence of elongated shadows on the surface provided the possibility of identifying even smaller boulders (2 pixels, i.e. 0.5 m in size, see Table 2). However, we considered the minimum diameter to be 1.75 m, as the SFD below this value starts to roll over, indicating that the sampling might not be complete **(see section 4 for a detailed discussion)**.

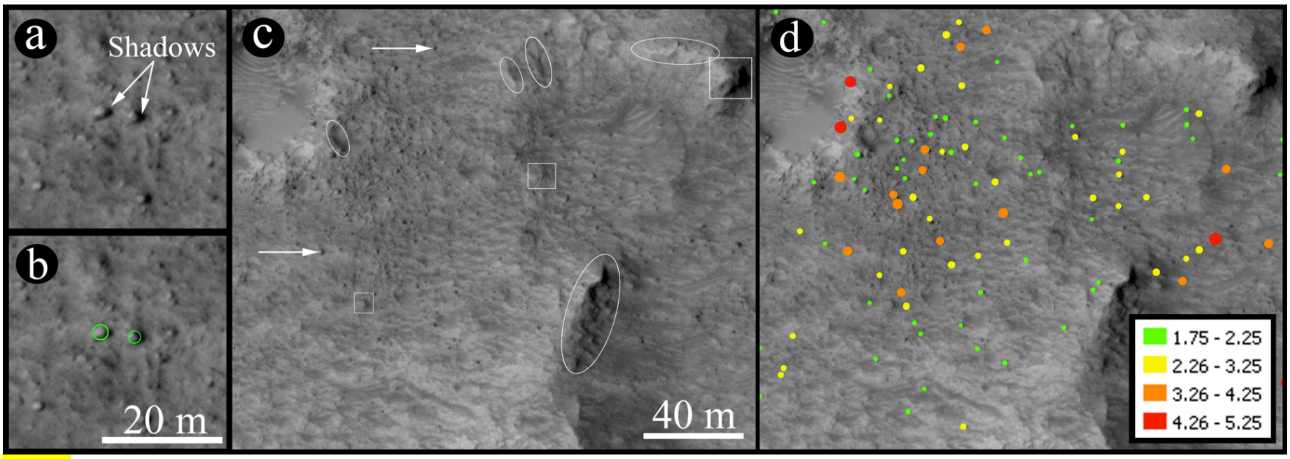

Fig. 3: Methodology used to identify two boulders located on the surface of Mars. A) Close-up of a set of boulders. The casted shadows are indicated with white arrows. B) Same as A, but with the fitted circles located at the terminators of the two boulders and partially overlapping the shadows. C) Subframe of the HiRISE image used in our analysis. The white arrows indicate the direction of the sunlight. The white ellipses indicate scarps and ledges of different sizes, while the white squares show hills/mounds with different dimensions. D) The detected boulders ≥ 1.75 m, grouped in size-categories (m).

3.0 Geological analysis

3.1 Geological mapping

A geological analysis based on bibliographic data, as well as on geomorphological observations, has been carried out over the study area. The geologic units were mapped on the basis of surface texture, relief, and albedo. We made use of both high-resolution imaging (i.e. **orthorectified** HiRISE image), coupled with DTM elevations (MOLA, CTX and HiRISE-based, Fig. 1) and the slope map **derived from** the HiRISE DTM at 1 m length scale (Fig. 2). Mineralogical analyses have been performed in the Oxia Planum region **(e.g. Carter et al., 2015a,b, 2016, Quantin et al., 2016)** and, even if these studies did not focus on our studied area, such data have been used to strengthen our interpretation. The resulting geological map, presented in Fig. 4, follows the criteria routinely adopted for planetary geological mapping (Hansen, 2000). This section is intended to constitute a basis for the boulder analysis and interpretation. Any speculation on geological processes that lead to the deposition of the identified units has been avoided, since such formation processes are discussed in detail in a companion paper (Quantin et al., in preparation) focusing on the entire Oxia Planum as the next ExoMars 2020 landing site.

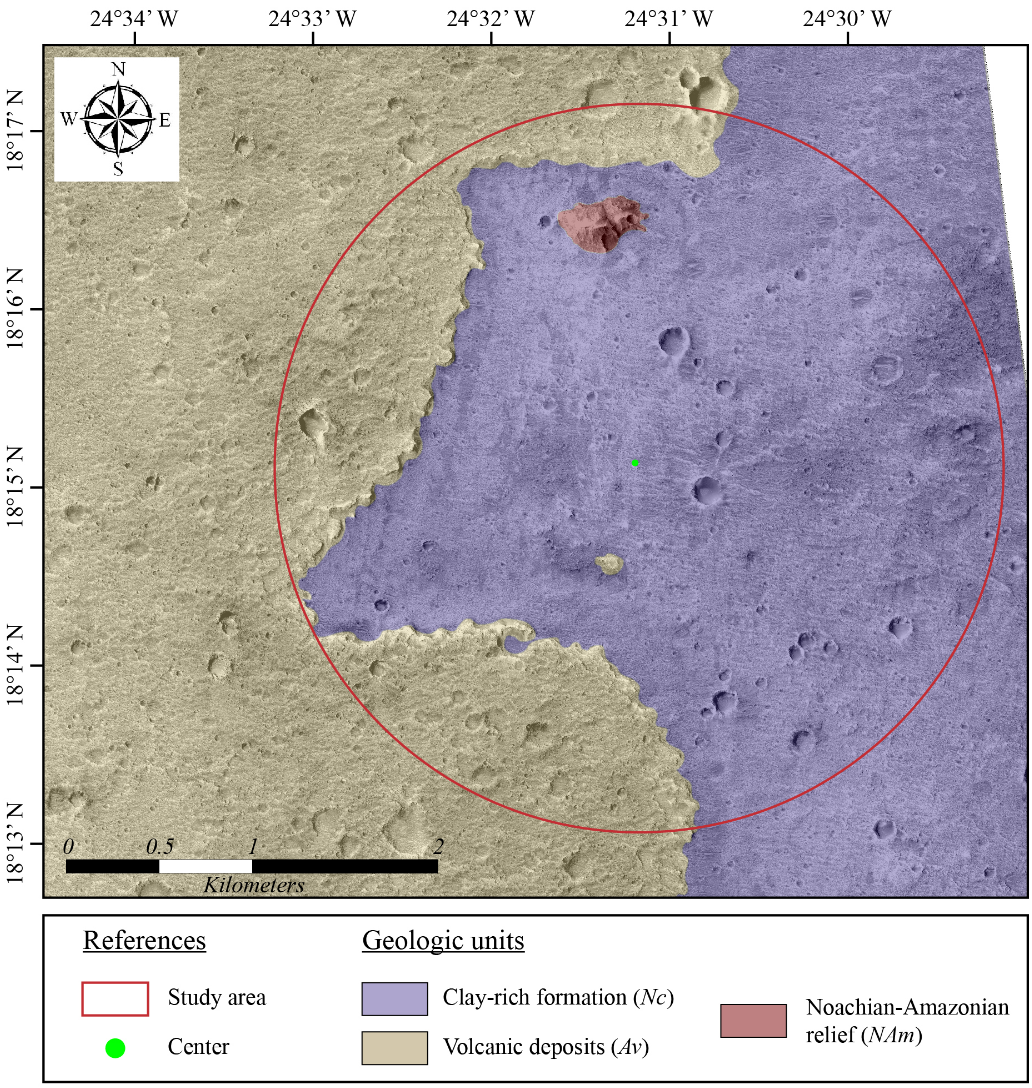

Fig. 4: Geological map of the study area showing the different identified units. The non-interpreted version of this figure is in Fig. 5a.

Three geological units have been identified (Fig. 4), and are here listed in stratigraphic order from the oldest to youngest, together with their prominent characteristics:

- Noachian clay-rich formation (Nc): this light-toned unit constitutes the majority of the study area, **outcropping** within the eastern sector of the study area and in large parts of the Oxia Planum region (Carter et al., 2015a, 2016; Ciarletti et al., 2015; Loizeau et al., 2015a; Quantin et al., 2015; Quantin et al., 2016). This unit presents a smooth texture at the HiRISE resolution (Fig. 5, detail 1) and is characterized by generally gentle slopes (Fig. 2),

excepting the flanks of the craters. It can be subdivided morphologically into two main homogeneous regions: the eastern plateau and the western lowlands. The plateau is located almost entirely above -2982 m MOLA and is connected to the low-lying western part by a gentle (about 7-14° inclined) slope. As can be appreciated in Fig. 2b, the lowlands are remarkably smoother than the plateau, with slope values never exceeding 7°.
Several patches of wind-blown deposits can be found on the surface of this unit, in particular in the lowlands (see Fig. 5b, detail 5, Fig. 6 and paragraph 3.3) and a continuous belt of scree material can be found next to the sharp scarp (Fig. 5b, detail 6) that bounds this unit to the west. Multiple studies (e.g. Carter et al., 2015a,b, 2016; Quantin et al., 2016) point out the presence of hydrated minerals in this unit, with a widespread occurrence of Mg/Fe phyllosilicates, consistent with either vermiculites or smectite-bearing mixed-layered clays. This unit has been found to date back to the Middle Noachian (3.9-4 Ga; Quantin et al., 2016) and has experienced various resurfacing events that lead to a Late Amazonian exposure age (~100 Ma; Quantin et al., 2016).

- Amazonian volcanic deposits (Av): this unit **outcrops** in the western sector of the study area, next to the Nc unit, from which **it** is separated by an abrupt scarp (40° to 60° inclined and 10 to 20 m high, see Fig. 1, 2b and 5b, detail 6) the base of which is at an elevation of about -2982 m MOLA. The Av unit is remarkably darker than the Nc one, and presents an extremely rugged surface at the HiRISE resolution. Sharp crests alternate to small depressions (Fig. 5b, detail 2), visible both in the images and in the slope map (Fig. 2). Compared to the previous unit, a larger quantity of craters and a much higher number of boulders is present (boulder density is more than 7.0 times higher, see section 4 for details). No mineralogical signatures of hydrated minerals have been found here. Indeed, this unit is **interpreted** to be basaltic lava flows, **due to the presence of morphologies related to effusive volcanism and to the absence of a hydration signature (Quantin et al., 2016). It** locally **covers** the underlying stratigraphic succession, protecting it from the effects of erosive processes and meteor impacts. Previous studies date the deposition of this unit to the Early Amazonian era (i.e. 2.6 Ga; Quantin et al., 2015, Quantin et al., 2016) and suggest that it has been remarkably eroded since its deposition. Given that this unit overlies the Nc one, it is likely that thin patches of Av may still **be** present on top of the older unit. This is surely the case for the isolated outcrop **located** south of the center of the study area, but may **also be the case for** the darker areas scattered on the Nc unit (Fig. 5b, detail 4). However, since the identification is **uncertain**, we prefer to include such areas in the older geological unit (see Fig. 4).

- Noachian-Amazonian **mound** (**NAm**): **this is a geological inconsistency with respect to the two main units presented above. It is** a **mound with** high relief (about 50 m high) and sharp scarps that connect it to the Nc unit. It appears to be dissected in the middle by a deep incision (Fig. 5, detail 3) with **steep** flanks. This geological element appears to be different from the previous units and it has been distinguished from them, in order to avoid any bias in the boulder analyses. Unfortunately, the flanks surrounding this outcrop are covered by aeolian and scree deposits and it is not possible to assess if it lays on top of the Nc unit, thus possibly being a remnant of the Av unit, isolated by erosional processes, or it belongs to a stratigraphically lower (and older) geological unit.

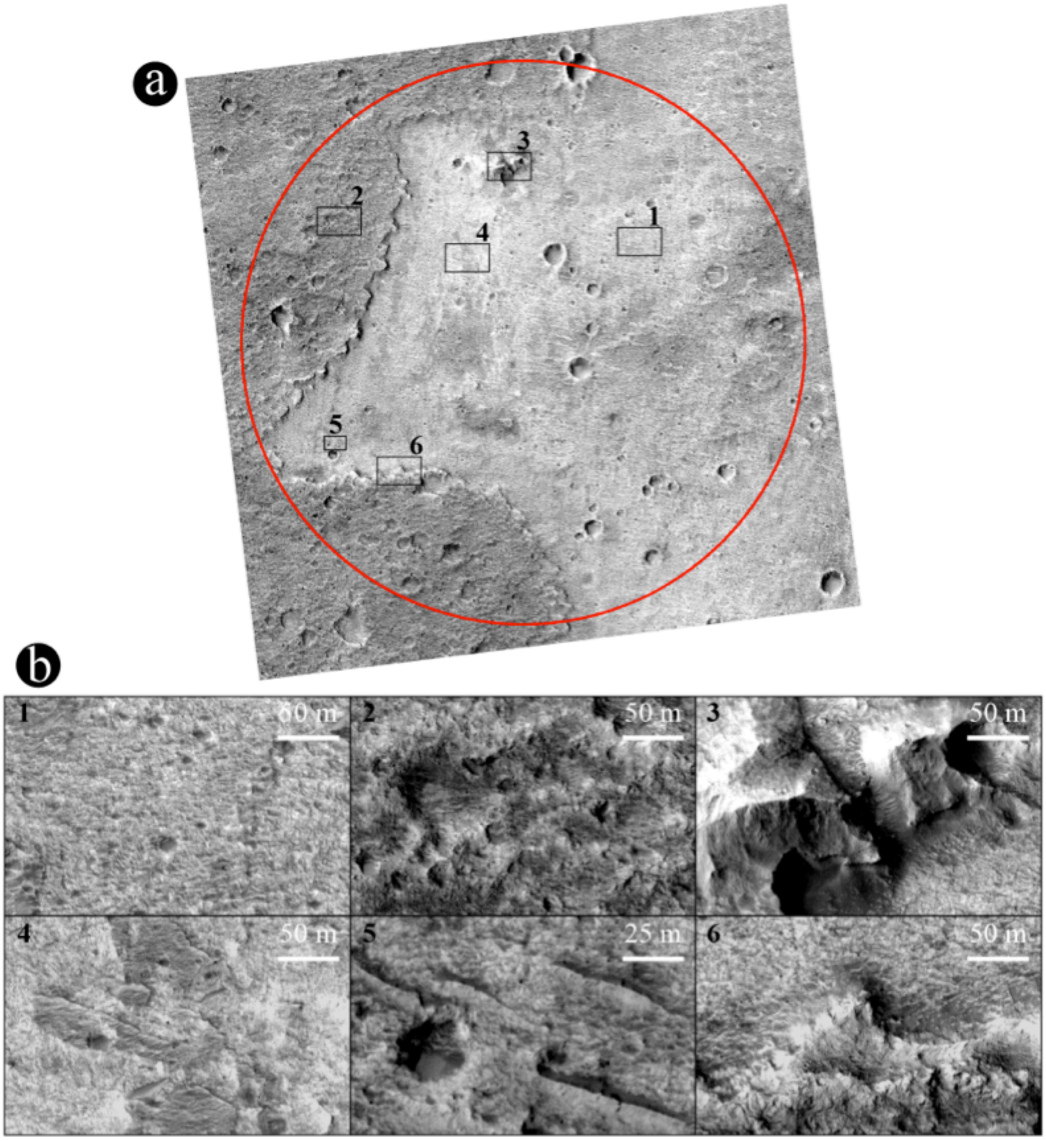

Fig. 5: (a) HiRISE image of the study area with the location of the underlying close-up images (b) HiRISE close-ups; all of them have been taken from the same image, at the same zoom (exception made for detail 5, **which** has a 2x zoom) and with the same stretching conditions, in order to allow visual comparisons of both textures and color tones. 1: Nc unit: the smooth texture of the terrain is easily perceivable, as well as its light tone; 2: Av unit: rugged textures of the terrain and dark tone are distinctive characteristics of this unit; 3: **NAm** unit: the central fracture and almost vertical flanks of this outcrop, surrounded by the Nc unit, are clearly visible in the close up; 4: darker patches of rock in the Nc unit, possibly constituting a thin layer of Av unit that survived the erosion; 5: 2x zoom image of aeolian ridges; it is possible to note some boulders lying on these deposits; 6: small section on the sharp scarp that separate the Nc unit from the Av one; it is here possible to notice a belt of mixed scree and aeolian sediments that accumulates at the foot of the scarp (northern side, in this image).

2 Fine-grained material distribution

The **accumulation** of fine-grained (particles <0.25 m) material **due to wind and/or gravity-related phenomena** can potentially cover boulders, biasing the results. Fig. 6 shows the distribution of all deposits that appear to be **formed from** such sediment. These deposits may **represent** aeolian material, such as aeolian ridges (Fig. 5b, detail 5) or scree sediments that accumulate at the base of the scarps (Fig. 5b, detail 6). However, since scarps are efficient obstacles to wind flow, these latter deposits are probably mixed in origin. **As can be seen in Figs. 2, 4, and 5, at the main boundary between the Av and Nc unit an almost continuous belt of such debris fields is present.**

We identified deposits covering a total area of 1.59 km^2 (i.e. 12.65% of the total analyzed surface, and 14% and 9% of the Nc and Av units respectively) (Fig. 6). Despite the potential obscuring effect of these deposits, we were still able to identify boulders laying on them (Fig. 5b, detail 5). Therefore, we believe that our boulder identification is not significantly biased and a meaningful size-frequency distribution analysis can be computed.

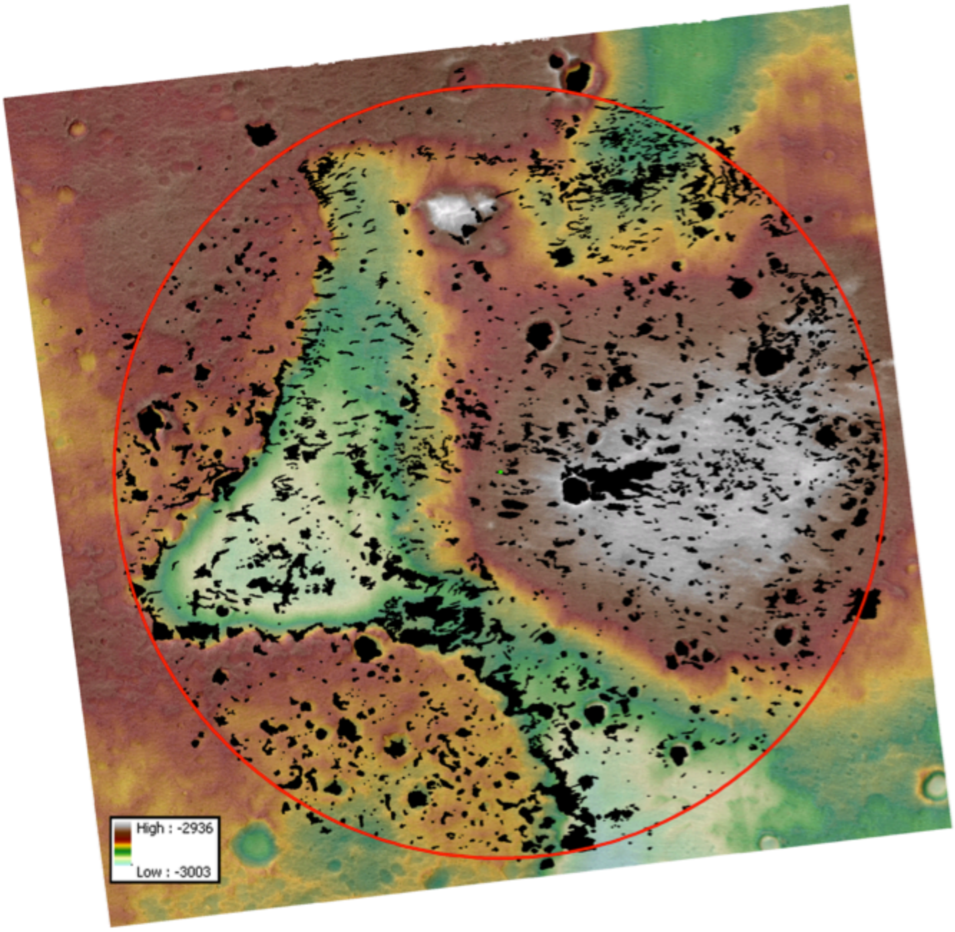

Fig. 6: **Fine**-grained material distribution over the study area (black areas).

4.0 SFD results

4.1 The entire study area

Over the entire study area (12.57 km^2) we identified 27,625 boulders ≥ 0.50 m, 8489 of which **are ≥ 1.75 m across**. The corresponding density of boulders ≥ 1.75 m per m^2 is 6.75×10^{-4}. Table 2 presents the statistics of the collected boulders, grouped in bins of 0.25 m, i.e. the HiRISE image resolution.

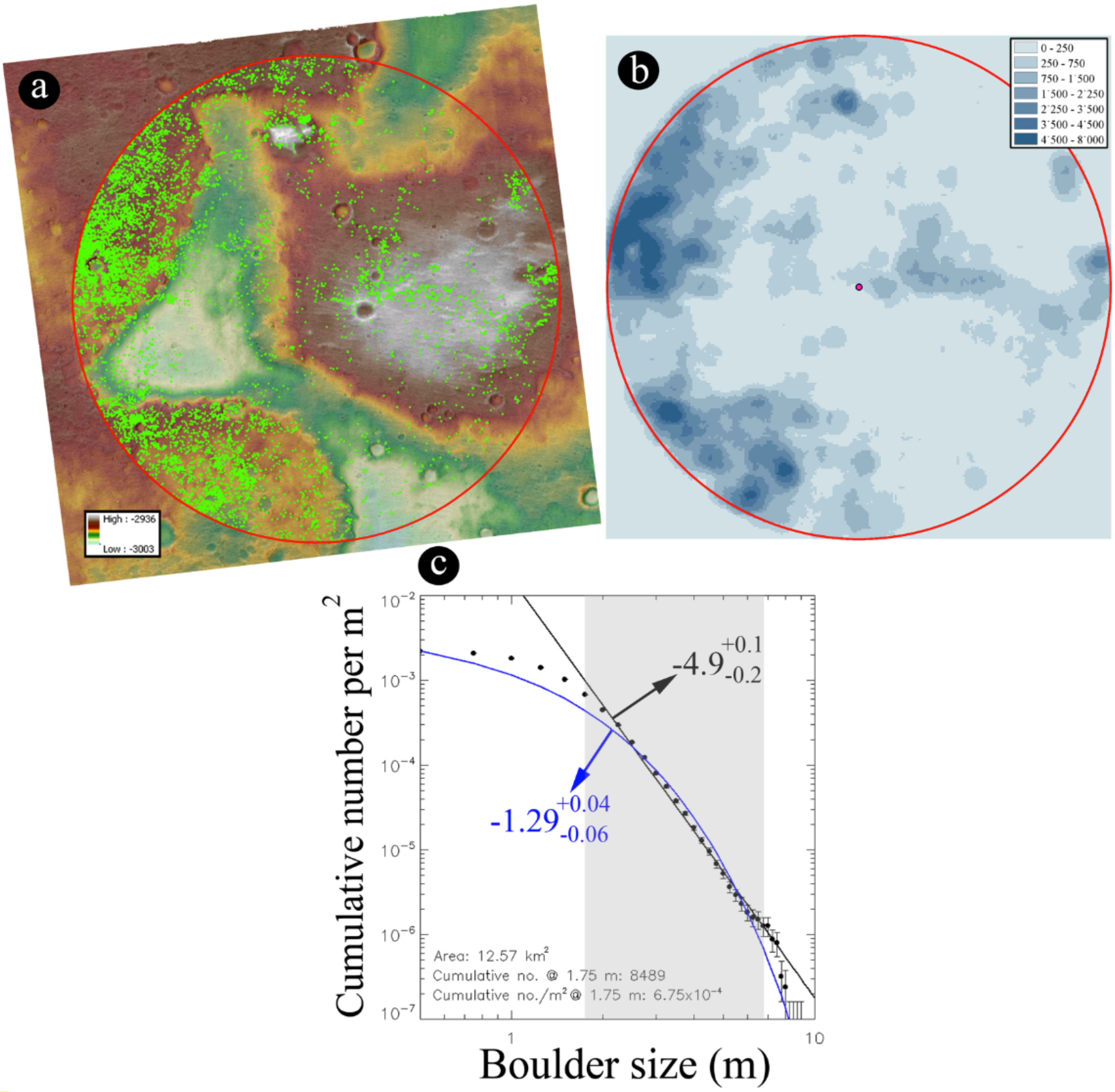

Fig. 7: (a) Spatial distribution of all the identified boulders ≥ 1.75 m **(green dots, detected on original HiRISE image and then reprojected onto the orthorectified one)** within the study area (12.57 km^2). (b) Density map of boulders in the study area. It is worth noting that the highest values are reached in the western sector, over the Av geological unit. In the Nc unit the highest densities are found in the eastern side of a large crater, near the center of the study area. (c) SFD of the identified boulders (bin size 0.25 m, Table 2). According to Michikami et al., 2008, vertical error bars indicate the root of the cumulative number of **counted** boulders divided by the considered area. **The data were fitted with a linear regression (solid black line) and with an exponential curve (solid blue line) performed in the 1.75 - 6.75 m interval (highlighted in grey).**

Fig. 7a shows the spatial distribution of all the identified boulders ≥ 1.75 m overlaid **and rectified** on the HiRISE DTM, while Fig. 7b shows how the rock density varies across the studied area. **Spatial densities (number of boulders per m^2) have been calculated over the study area with a mobile circular cell (250 m radius) and subdivided into seven classes. The highest values are reached in the western sector, over the Av geological unit. In the Nc unit a peak in the density values is found in the eastern side of a large crater, near the center of the study area.**

The cumulative boulder SFD per m^2 of the entire area is shown in Fig. 7c. **Both the power-law and the exponential-law fitting curves** used to interpolate the number of boulders per m^2 **take** into account those boulders **within the 1.75 - 6.75 m diameter range**. **The power-law index derived from the total amount of boulders ≥ 1.75 m is -4.9 +0.1/- 0.2 (Fig. 7c black line) with a coefficient of determination (R^2) equal to 0.992. The fitting exponential curve has an exponent**

of -1.29 +0.04/- 0.06 and a R^2 value of 0.980 (Fig. 7c blue curve). These results suggest that in the selected range both power and exponential models provide good fits to the data.

As described above, for the statistical analysis we considered the smallest diameter to be 1.75 m across. Below this value, the power-law model overestimates the sizes while the exponential model underestimates them (regression lines are above/under the data, respectively). As suggested in other studies (e.g. Heet et al 2009, Hebrard et al 2012), the observed cumulative distribution flattens at sizes smaller than ~1.5 m due to the resolution limit of the image. At that diameter size, the power-law model tends to overestimate the smaller diameter boulders, while the flattening of the exponential distributions allows a better representation of the distributions of such boulders (Golombek et al 2008, Hebrard et al 2012). Following Michikami et al., (2008) and Pajola et al., (2015, 2016d), we do not consider such boulders larger than 6.75 m in diameter, since the presence of the same cumulative number in subsequent values is an indication of poor statistics. Such values, typically the bigger boulder sizes, should not be considered by the fit to avoid misinterpretations. In fact, **sizes greater than 6.75 m are slightly overestimated by the power-law model while clearly underestimated by the exponential one.**

These considerations apply to all size-frequency plots presented in this paper.

Table 2: Statistics of the identified boulders, grouped per bin (0.25 m wide). The grey rows show the size range of the boulders considered in the statistical analysis of Fig. 7.

Bin* [m]	Absolute frequency	Cumulative number**	Cumulative number/m^2
0.50	1480	27625	2.20×10^{-3}
0.75	3399	26145	2.08×10^{-3}
1.00	5048	22746	1.81×10^{-3}
1.25	4892	17698	1.41×10^{-3}
1.50	4317	12806	1.02×10^{-3}
1.75	2890	8489	6.75×10^{-4}
2.00	1869	5599	4.45×10^{-4}
2.25	1391	3730	2.97×10^{-4}
2.50	796	2339	1.86×10^{-4}
2.75	536	1543	1.23×10^{-4}
3.00	303	1007	8.01×10^{-5}
3.25	230	704	5.60×10^{-5}
3.50	136	474	3.77×10^{-5}
3.75	109	338	2.69×10^{-5}
4.00	67	229	1.82×10^{-5}
4.25	41	162	1.29×10^{-5}
4.50	35	121	9.63×10^{-6}
4.75	20	86	6.84×10^{-6}
5.00	20	66	5.25×10^{-6}
5.25	9	46	3.66×10^{-6}
5.50	8	37	2.94×10^{-6}
5.75	6	29	2.31×10^{-6}
6.00	3	23	1.83×10^{-6}
6.25	1	20	1.59×10^{-6}
6.50	3	19	1.51×10^{-6}
6.75	0	16	1.27×10^{-6}
7.00	5	16	1.27×10^{-6}
7.25	1	11	8.75×10^{-7}
7.50	6	10	7.96×10^{-7}
7.75	1	4	3.18×10^{-7}

8.00	2	3	2.39×10^{-7}
8.25	0	1	7.96×10^{-8}
8.50	0	1	7.96×10^{-8}
8.75	0	1	7.96×10^{-8}
9.00	1	1	7.96×10^{-8}

* the column reports the lower limit of each bin; ** the cumulative number is intended as the number of boulders with dimension equal to or greater than the selected lower limit (i.e. first column).

4.2 Localized areas

The **lithology** of single boulders could be inferred neither from visual examination nor mineralogical data due to their limited dimensions. A transport origin should be considered as a possible factor for boulder deposition, but the problem with this hypothesis is that the aeolian transport is not admissible, since it requires an unrealistic amount of energy to move clasts such as those considered in this study. A fluvial/glacial environment can be suggested, but the closest fluvio-deltaic deposits identified so far in the Oxia Planum region are located more than 30 km to the south east of the study area, at the outlet of Cogoon Vallis (Quantin et al., 2016). When all such aspects are taken into account, it is likely that the considered boulders are composed **of** the same lithology **as** the geological unit **that** they **overlie**. Moreover, the analysis of terrestrial crater ejecta suggests that large clasts derive from near surface regions, whilst the smaller ones **originate from** deeper levels (Kumar et al., 2014): therefore, by considering the size of the boulders involved in our study (i.e. ≥ 1.75 m), we suggest that most of them come from the near surface, corroborating our *a-priori* assumption.

Following the geological analysis (Fig. 4), we grouped those boulders located on the Av and Nc unit, to investigate if any differences in SFD are present between boulders belonging to different geological units. On the 3.29 km^2 Av unit, the cumulative number of boulders ≥ 1.75 m **across** is 5881, with a density value of 1788 boulders/km^2, Table 3. **Conversely, the cumulative number of boulders ≥ 1.75 m across identified on the 8.97 km^2 Nc unit is 2285, with a density value of 2.55×10^{-4} boulders/m^2. In the Av unit, the fitting power-law curve has an index of -4.8 +/- 0.2 (R^2 = 0.996) (Fig. 8a black line), whereas the exponential-law curve shows an exponent of -1.24 +0.05/- 0.06 (R^2 = 0.981) (Fig. 8a blue curve). The Nc unit (Fig. 8b), shows a power-law index of -5.5 +0.3/-0.4 (R^2 = 0.985) and an exponential model with an exponent of -1.70 +0.09/- 0.12 (R^2 = 0.996).**

As for the entire studied area, the results show a good agreement between the power-law/exponential-law curves and the data within the fitting ranges. The power-law model again overestimates the size of boulders both below and above the fitting ranges, in both units. The exponential fit shows an underestimation of the diameters < 1.75 in the Av unit and a small overestimation for the same sizes in the Nc unit. As previously observed (Fig. 4), the distributions of the data tend to flatten at smaller boulder sizes (~1.5 m). Again, this is a result of the resolution limit of the images used to derive the distributions (e.g. Heet et al 2009, Hebrard et al 2012). As previously discussed, the exponential-law curve that is curved in a log-log plot tends to better represent the flattening of the distribution at small sizes when compared to the power-law fit.

We point out that a large crater (diameter = 230 m) is located within the Nc unit (Fig. 8, black arrows), clearly surrounded by radial ejected boulders. This feature, remarkably larger than other craters in the study area, may have locally increased the density of boulders and, therefore, the **mean** Nc boulder density over larger sectors may be even smaller than that one obtained in our case. Consequently, **the ratio between the boulder densities of the Av and the Nc unit may be even greater than the measured value of 7.0. Due to the high uncertainties and possible biases**

that would derive from a manual removal of boulders connected to this feature, we decided not to exclude them.

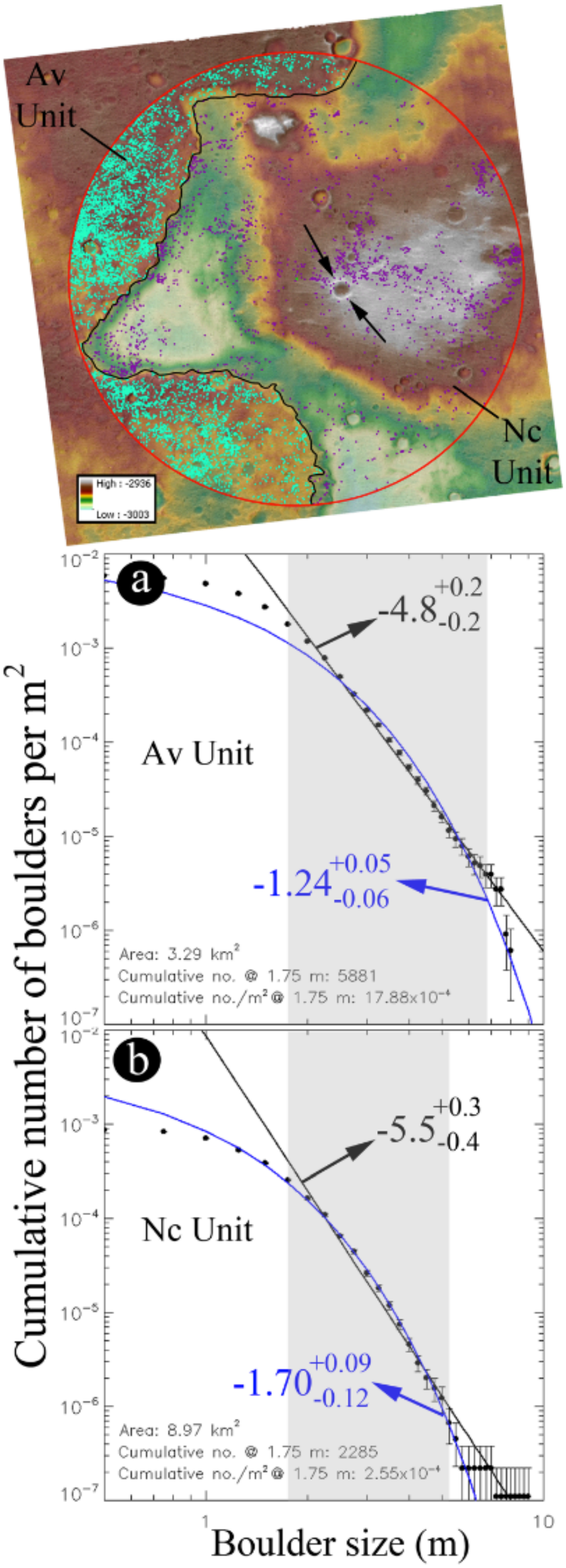

Fig. 8: Uppermost panel: HiRISE DTM showing the spatial distribution of all boulders detected, **grouped according to the geologic units**. **Those located on the Av unit are shown in light-blue, whilst those on the Nc unit are shown in purple**. Black arrows in **the** top panel show the location of the crater referred **to** in the text. **The cumulative SFDs for both regions are presented in a) and b). The data were fitted with a linear regression (solid black line) and with an exponential curve (solid blue curve) performed on data between 1.75 and 6.75 m on the Av unit and between 1.75 and 5.25 on the Nc unit (the fitting ranges are highlighted in grey) as shown in Fig. 7.**

Table 3: Statistics of the identified boulders, grouped per bin (0.25 m wide) over the Av and the Nc units, respectively. The grey rows show the size ranges of the boulders considered in the statistical analysis of Fig. 9.

Av Unit

Bin* [m]	Absolute frequency	Cumulative number**	Cumulative number/m^2
0.50	1125	19347	5.88×10^{-3}
0.75	2297	18222	5.54×10^{-3}
1.00	3420	15925	4.84×10^{-3}
1.25	3529	12505	3.80×10^{-3}
1.50	3095	8976	2.73×10^{-3}
1.75	2001	5881	1.79×10^{-3}
2.00	1304	3880	1.18×10^{-3}
2.25	944	2576	7.83×10^{-4}
2.50	571	1632	4.96×10^{-4}
2.75	346	1061	3.23×10^{-4}
3.00	216	715	2.17×10^{-4}
3.25	154	499	1.52×10^{-4}
3.50	92	345	1.05×10^{-4}
3.75	75	253	7.69×10^{-5}
4.00	48	178	5.41×10^{-5}
4.25	30	130	3.95×10^{-5}
4.50	30	100	3.04×10^{-5}
4.75	17	70	2.13×10^{-5}
5.00	15	53	1.61×10^{-5}
5.25	7	38	1.16×10^{-5}
5.50	5	31	9.42×10^{-6}
5.75	6	26	7.90×10^{-6}
6.00	3	20	6.08×10^{-6}
6.25	1	17	5.17×10^{-6}
6.50	3	16	4.86×10^{-6}
6.75	0	13	3.95×10^{-6}
7.00	4	13	3.95×10^{-6}
7.25	0	9	2.74×10^{-6}
7.50	6	9	2.74×10^{-6}
7.75	1	3	9.12×10^{-7}
8.00	2	2	6.08×10^{-7}

Nc Unit

Bin* [m]	Absolute frequency	Cumulative number**	Cumulative number/m^2
0.50	353	7798	8.69×10^{-4}
0.75	1088	7445	8.30×10^{-4}
1.00	1599	6357	7.09×10^{-4}
1.25	1310	4758	5.30×10^{-4}
1.50	1163	3448	3.84×10^{-4}
1.75	815	2285	2.55×10^{-4}
2.00	494	1470	1.64×10^{-4}
2.25	395	976	1.09×10^{-4}
2.50	182	581	6.48×10^{-5}
2.75	165	399	4.45×10^{-5}
3.00	71	234	2.61×10^{-5}
3.25	56	163	1.82×10^{-5}
3.50	40	107	1.19×10^{-5}
3.75	26	67	7.47×10^{-6}
4.00	15	41	4.57×10^{-6}
4.25	8	26	2.90×10^{-6}
4.50	4	18	2.01×10^{-6}
4.75	3	14	1.56×10^{-6}
5.00	5	11	1.23×10^{-6}
5.25	2	6	6.69×10^{-7}
5.50	2	4	4.46×10^{-7}
5.75	0	2	2.23×10^{-7}
6.00	0	2	2.23×10^{-7}
6.25	0	2	2.23×10^{-7}
6.50	0	2	2.23×10^{-7}
6.75	0	2	2.23×10^{-7}
7.00	1	2	2.23×10^{-7}
7.25	0	1	1.12×10^{-7}
7.50	0	1	1.12×10^{-7}
7.75	0	1	1.12×10^{-7}
8.00	0	1	1.12×10^{-7}
8.25	0	1	1.12×10^{-7}
8.50	0	1	1.12×10^{-7}
8.75	0	1	1.12×10^{-7}
9.00	1	1	1.12×10^{-7}

* the column reports the lower limit of each bin; ** the cumulative number is intended as the number of boulders with dimension equal to or greater than the selected lower limit (i.e. first column).

4.3 Sensitivity analysis

To provide information on the sensitivity of the presented results to the size of the detected boulders, we performed a numerical simulation randomly changing the diameter of such boulders within selected ranges. We adopted the same technique presented in Baratti et al., 2015 and Pajola et al., 2017. The experiment was separately performed for *(i)* the whole sample of the detected boulders, *(ii)* for the boulders detected on the Av and *(iii)* for the boulders detected on the Nc units.

As a first step, each detected diameter was independently perturbed by adding a value extracted from uniform distributions in the ranges ±0.125, ±0.25 and ±0.50 m (i.e. corresponding to half, one and two pixels of the used HiRISE image). Later, the boulder diameters were binned using the same lower and upper bin limits reported in the first columns of tables 2 and 3 (i.e. increasing step of 0.25 m). Finally, the SFDs' power-law and exponential-law fits were recomputed in the same range of diameters previously adopted (i.e. 1.75-6.75 m for the whole area and the Av unit, and 1.75-5.25 m for the Nc unit).
In each case we performed 10^5 simulations. The experiment was performed in order to provide information about the accuracy and the overall objectivity of the detected diameters and the results. **The maximum selected perturbation of two pixels is based on the assumption that in our manual detection we consider unlikely an error of over- or underestimation greater than 2 pixels. Indeed, as suggested by Golombek et al. (2008), the accuracy in the manual detection of boulders (in a MOC image) is within ±1 pixel. Thus, although this conclusion may be questionable, we retain that our maximum adopted perturbation (i.e. ±2) is conservative.**

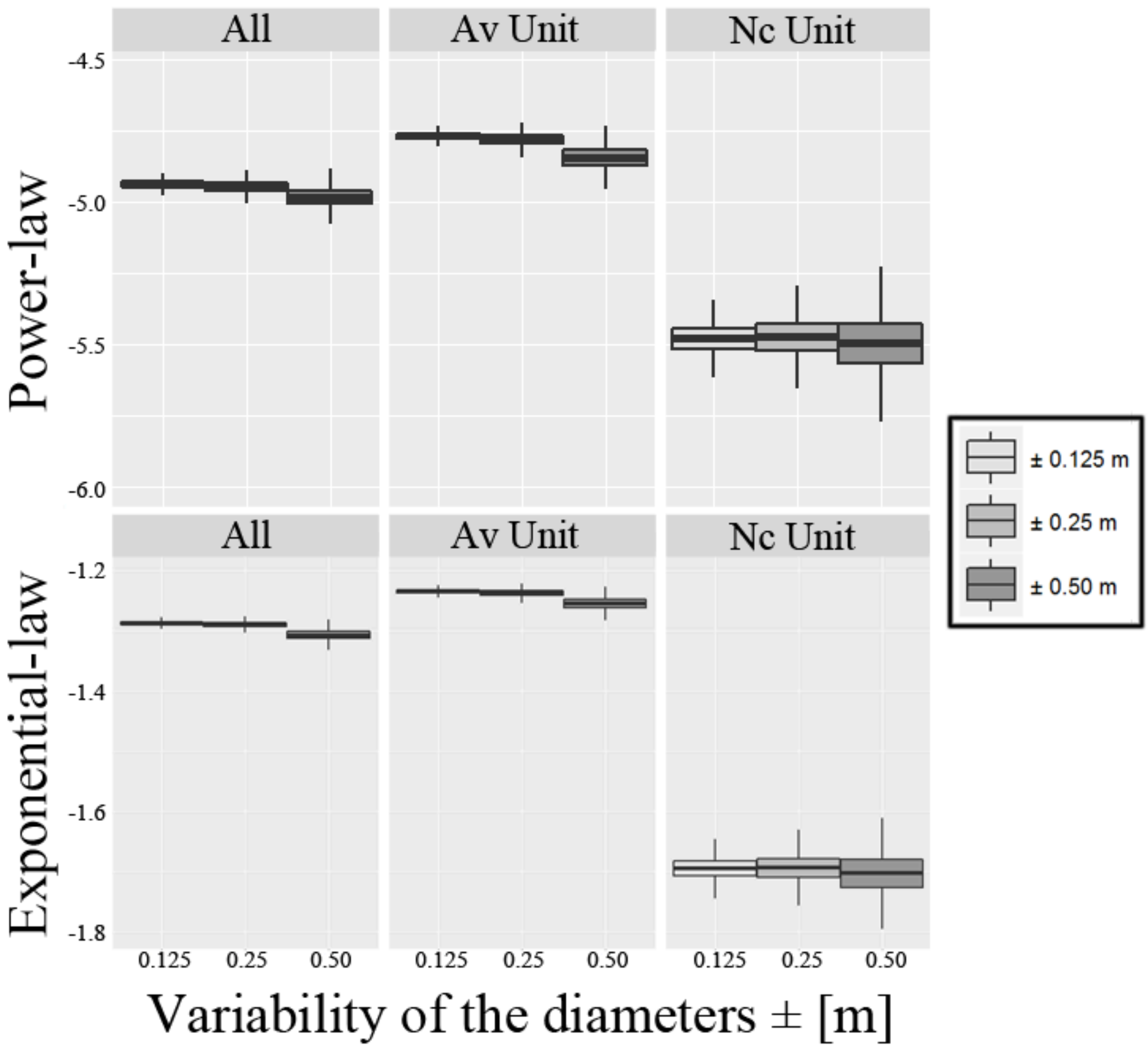

Fig. 9: Sensitivity analysis - box plot of **the power-law and exponential-law indices obtained** by varying the size of the identified boulders by ±0.125, ±0.25 and ±0.50 m (i.e. half, one and two pixels). The upper and lower hinges correspond to the 25th and 75th percentiles; the whiskers extend from the minimum to the maximum values.

The results obtained are presented in Fig. 9. Both fitting models (power-law and exponential-law) show for all units increased variability in the indices with an increasing range of the selected perturbations. A higher sensitivity of the results is found for the boulders in the Nc unit, as we expected due to the smaller amount of boulders used for this unit (2285), compared to the Av one (5581) and to the entire region (7866). Nonetheless, the Av unit shows power-law and exponential-law indices that are always greater than the Nc one, with values ranging between -4.75 ÷ -5.00 and -1.22 ÷ -1.28 compared to -5.25 ÷ -5.75 and -1.6 ÷ -1.8 for the Nc unit (power-law and the exponential-law curves, respectively). Regarding the median values, all results are coherent with those previously presented (Fig. 7, 8).
This analysis supports the hypothesis that each boulder group is characterized by power-law and exponential-law indices that are different from the other ones.

4.4 Boulder measurement uncertainties

Our analysis is prone to several assumptions and sources of uncertainty. Errors and uncertainties in determining the boulder shape from shadows depend, for instance, on the solar incidence angle and on the height of the boulder (Golombek et al. 2008). For a given boulder, the greater the Sun angle above the horizon, the smaller its shadow, until the Sun is directly overhead, not allowing any shadow to form. Uncertainty in the identification of boulders can also derive from ambiguity in the location of the shadow penumbra where the direct to indirect illumination transition occurs (for details see, for instance, Golombek et al 2008).
Other papers have presented reliable results with Sun angle values of, for instance, 41° (MOC images, Golombek et al 2008), 31.5° and 33.3° (HiRISE images, Golombek et al. 2008) and about 36° in Golombek et al. (2012). In our case, as shown in Fig. 3a and 3b, the incidence angle is 48°, allowing reliable identification of shaded and non-shaded regions, and therefore of the boulders themselves.

Other sources of uncertainty in our analysis are those related to the ability to differentiate non-boulder features that cast shadows (such as portions of escarpments, small hills, and mounds) from real boulders, and to the resolution of the images. Given that the boulders were manually detected, we consider the uncertainty related to the differentiation of boulders from other features to be low, compared to the uncertainties related to the resolution of the images. For instance, Golombek et al. (2012b), by using an automated boulder counting algorithm that fits ellipses to shadows and cylinders to the rocks, show that boulders >1.5 m diameter are fully resolvable in HiRISE images. The authors discuss the limited capability of the automated process to differentiate non-boulder features that cast shadows and the importance of visual inspection of automatically detected boulders by operators in order to exclude non-boulders from the maps. In our analysis, the map-projected HiRISE image resamples the pixels to create a consistent pixel scale of 25 cm/pixel, introducing uncertainties in the estimation of the real diameter. The smaller the boulder, the bigger the relative uncertainty is; nevertheless, in our statistical analysis we do not consider boulders with diameters <1.75 m (i.e. 7 pixels), corresponding to an area of ~2.7 m^2 (i.e. ~44 pixels). Moreover, we point out that, by manually identifying boulders in high-resolution MOC images (Malin et al., 1998) as pairs of light and dark pixels (bright and shaded sides) on the images, Golombek et al (2003) found that "although there was some uncertainty in the identification, it was generally repeatable, with different observers yielding similar results. Measured boulder diameter is probably within ±1 pixel". Such consideration, as well as the results of the sensitivity analysis, give us confidence on the robustness and reliability of our detection and identification of boulders and on the reliability of our results.

5.0 Discussion

5.1 Comparison with SFDs in the Solar system

In order to understand what the derived Oxia Planum SFDs mean, which processes produced them, and to contextualize them in the wider framework of Solar System SFD studies, we here summarize the literature on boulder size-distributions obtained through remote sensing i) on the Moon, ii) on asteroids, iii) on comets and iv) on Mars. We point out that there is a vast literature on Terrestrial fractal fragmentation as well, e.g. Hartmann (1969), Curran et al., (1977), Fujiwara et al. (1977), Wu et al., (1993), Turcotte (1997), Senthil Kumar et al., (2014), but with the exception of few cases where m-sized boulders are considered, such as Bennet (1936) and Schoutens (1979), all the presented power-law indices are derived from laboratory fragmented pebbles, hence with diameters ranging from mm to dm, but never reaching the dimensions we identified on Oxia Planum. For this reason we cannot use them as a possible Oxia Planum comparison.

On the Moon, there is important literature regarding different SFD power-law indices derived from orbital imaging. The considered size-ranges are equal or comparable (1 to 50 m across) to the ones used on Oxia Planum, hence they can be used as a comparison to our analysis (Table 3). By using Lunar Orbiter images, Cintala and McBride (1995) have analyzed the debris fields surrounding the Surveyor I, II, VI and VII landing sites (Shoemaker and Morris (1970) and Hartmann (1969)). The resulting power-law indices range between -3.51 (Surveyor I landing site, evaluated in the 1-5 m range) and -6.02 (Surveyor VI landing site, evaluated in the 1-4 m range). Bart and Melosh (2010) presented a wide dataset of power-law indices that were derived for several lunar craters using NASA Lunar Orbiter III, V and the Apollo 17 dataset and evaluated in a size-range of 3 to 50 m. The power-law curves Bart and Melosh (2010) used to fit the SFD have indices ranging between -3.0 to -4.5, with a single best fitted case of -5.5. By using the Lunar Reconnaissance Orbiter (LRO) images, Krishna and Senthil Kumar (2016) identified a power-law index of -2.76 derived from the boulders in the 2-25 m range surrounding the Censorinus crater.
All the presented SFDs have been attributed to impact related processes since such indices, and the shapes of the fragments (when available), reflect the distributions produced by impact of a rock surface on the ground (Surveyor Scientific Evaluation and Analysis Team (1966a), Shoemaker, 1965; Melosh 1984, p. 254). The steepest power-law indices obtained on the Moon are derived through size ranges comparable to those identified in the Oxia Planum landing site and can be therefore considered as a crater-related fracturing reference for our distributions.

Table 3: The SFD derived for lunar boulders and the corresponding size range at which they were derived.

Moon:	Mission	Reference	Power-law index	Diameter size/Range	Notes
Surveyor I landing site	NASA/Lunar Orbiter	Cintala and McBride (1995)	-3.51 ± 0.47	1 - 5 m	Field debris surrounding Surveyor I landing - impact related
Surveyor III landing site	NASA/Lunar Orbiter	Cintala and McBride (1995)	-5.65 ± 0.63	1 - 6.5 m	Field debris surrounding Surveyor III landing - impact related
Surveyor VI landing site	NASA/Lunar Orbiter	Cintala and McBride (1995)	-6.02 ± 1.40	1 - 4 m	Field debris surrounding Surveyor VI landing - impact related
Surveyor VII landing site	NASA/Lunar Orbiter	Cintala and McBride (1995)	-4.03 ± 0.14	10 - 65 m	Field debris surrounding Surveyor VII landing - impact related
Crater III-185-H3	NASA/Lunar Orbiter III	Bart and Melosh (2010)	-4.2	3 - 10 m	Collisional Impact related to crater III-185-H3
Crater III-168-H2	NASA/Lunar Orbiter III	Bart and Melosh (2010)	-4.0	4 - 18 m	Collisional Impact related to crater III-168-H2
Crater III-186-H3	NASA/Lunar Orbiter III	Bart and Melosh (2010)	-4.0	3 - 18 m	Collisional Impact related to crater III-186-H3
Crater III-189-H2	NASA/Lunar Orbiter III	Bart and Melosh (2010)	-3.0	4 - 15 m	Collisional Impact related to crater III-189-H2
Crater V-63-H2	NASA/Lunar Orbiter V	Bart and Melosh (2010)	-3.0	10 - 70 m	Collisional Impact related to crater V-63-H2
Crater V-82-M	NASA/Lunar Orbiter V	Bart and Melosh (2010)	-3.0	50 - 320 m	Collisional Impact related to crater V-82-M
Crater V-152-H2	NASA/Lunar Orbiter V	Bart and Melosh (2010)	-5.5	5 - 18 m	Collisional Impact related to crater V-152-H2
Crater V-153-H2	NASA/Lunar Orbiter V	Bart and Melosh (2010)	-3.0	5 - 45 m	Collisional Impact related to crater V-153-H2
Crater V-167-H2	NASA/Lunar Orbiter V	Bart and Melosh (2010)	-4.0	4 - 18 m	Collisional Impact related to crater V-167-H2
Crater V-167-H3	NASA/Lunar Orbiter V	Bart and Melosh (2010)	-4.0	5 - 20 m	Collisional Impact related to crater V-167-H3
Crater V-199-M	NASA/Lunar Orbiter V	Bart and Melosh (2010)	-2.2	50 - 380 m	Collisional Impact related to crater V-199-M
Crater V-211-H3	NASA/Lunar Orbiter V	Bart and Melosh (2010)	-4.0	4 - 18 m	Collisional Impact related to crater V-211-H3
Ap17-Pan-2345a	NASA/Apollo 17	Bart and Melosh (2010)	-4.0	10 - 40 m	Collisional Impact related to crater Ap17-Pan-2345a
Ap17-Pan-2345b	NASA/Apollo 17	Bart and Melosh (2010)	-4.5	10 - 30 m	Collisional Impact related to crater Ap17-Pan-2345b
Ap17-Pan-2345e	NASA/Apollo 17	Bart and Melosh (2010)	-4.5	10 - 22 m	Collisional Impact related to crater Ap17-Pan-2345e
Ap17-Pan-2345f	NASA/Apollo 17	Bart and Melosh (2010)	-4.0	10 - 30 m	Collisional Impact related to crater Ap17-Pan-2345f
Ap17-Pan-2345g	NASA/Apollo 17	Bart and Melosh (2010)	-4.5	10 - 30 m	Collisional Impact related to crater Ap17-Pan-2345g
Ap17-Pan-2345i	NASA/Apollo 17	Bart and Melosh (2010)	-3.2	10 - 50 m	Collisional Impact related to crater Ap17-Pan-2345i
Censorinus crater	NASA/LRO	Krishna and Senthil Kumar (2016)	-2.76	2-25 m	Collisional Oblique Impact related to Censorinus crater

When asteroids are taken into account, boulders or large blocks present on their surfaces are interpreted to be the result of impact processes as well. Indeed, they are considered to be the largest fragments excavated during the impact as they can always be found in close proximity to craters. In the case of the two asteroids (433) Eros and (25143) Itokawa, the high-resolution images **allowed derivation of** the SFD of boulders with sizes above 5 and 15 m respectively, returning a power-law index ranging between -3.1 and -3.5 (Michikami et al., 2008; Mazrouei et al., 2014), see Table 4. This range falls inside the one presented for the Moon, hence supporting an impact origin as well (Geissler et al., 1996, Thomas et al., 2001, Michikami et al., 2008, Mazrouei et al. 2014). Nevertheless, when bigger size ranges are considered on (433) Eros, i.e. from 80 to 105 m, a steeper -6.1 power-law index has been identified, but it has been explained by Dombard et al. (2010) as a result of possible depletion after an impact origin. In addition, Küppers et al., (2012) supported an impact related origin to the (21) Lutetia boulders, as a result of the north polar crater cluster implantation.

We point out that in all asteroidal cases, the derived power-law indices are lower than the ones we identified on Oxia Planum, with the only two cases of -6.1 on (433) Eros and -5.0 on (21) Lutetia, where the size ranges are remarkably larger than those considered in our work. In addition, these bodies have small-to-negligible surface gravity compared to that of Mars, so any comparison with Martian studies should exercise caution.

Table 4: The SFD derived for asteroid boulders and the corresponding size range at which they were derived.

Asteroids:	Mission	Reference	Power-law index	Diameter size/range	Notes
(433) Eros	NASA/NEAR	Thomas et al. (2001)	-3.2	≥ 15 m	Collisional impact related, Shoemaker crater
(433) Eros	NASA/NEAR	Dombard et al. (2010)	-3.1	10 - 80 m	Collisional impact related, Shoemaker crater
(433) Eros	NASA/NEAR	Dombard et al. (2010)	-6.1	80 - 105 m	Depletion during implantation after impact origin
(25143) Itokawa	JAXA/Hyabusa	Michikami et al. (2008)	-3.1 ± 0.1	≥ 5 m	Impact related, Itokawa formation scenario
(25143) Itokawa	JAXA/Hyabusa	Mazrouei et al. (2014)	-3.5 ± 0.1	≥ 6 m	Impact related, Itokawa formation scenario
(21) Lutetia	ESA/Rosetta	Küppers et al. (2012)	-5.0	60 - 300 m	Impact related, north polar crater cluster

A possible comparison can be made with cometary boulder SFD**s** that have **recently** been obtained **for comets** 103P Hartley 2 and 67P Churyumov-Gerasimenko. Indeed, it has been suggested **that** comets are affected by processes that are completely different with respect to impacts, such as sublimation, outbursts and gravitational falls, cliff regressive erosions, lifting and re-deposition (Pajola et al., 2015, 2016e,f, Mottola et al., 2015). A list of all power-law indices, the corresponding size ranges, and the related phenomena is presented in Table 5. From this table, it is possible to see how one of the steepest power-law **indices** observed on a Solar system body, i.e. between -5.0 to -6.5, is related to collapse/pit formation and consequent creation of depressions.

Despite similar power-law indices, the target rocks in Oxia Planum are much denser **than** the cometary ones, and they are not affected by solar radiation in such **an** extreme way. This means that our results are hardly comparable to cometary analyses.

Table 5: The SFD derived for cometary boulders and families and the corresponding size range at which they were derived.

Comets:	Mission	Reference	Power-law index	Diameter size/Range	Notes
103P Hartley 2	NASA/EPOXI	Pajola et al. (2015a)	-2.7 ± 0.2	10 - 40 m	Disintegration/fragmentation through sublimation, or lifting drag processes
67P Churyumov-Gerasimenko	ESA/Rosetta	Pajola et al. (2015b,e)	-3.6 ± 0.2	7 - 35 m	Gravitational events from regressive erosion
67P Churyumov-Gerasimenko	ESA/Rosetta	Pajola et al. (2015b,f)	-5.0 to -6.5	7 - 35 m	Collapse/pit formation and creation of depressions
67P Churyumov-Gerasimenko	ESA/Rosetta	Pajola et al. (2015b,f)	-3.5 to -4.5	7 - 35 m	Gravitational events from regressive erosion
67P Churyumov-Gerasimenko	ESA/Rosetta	Pajola et al. (2015b,f)	-1.0 to -2.0	7 - 35 m	Sublimation of not replenished cometary boulders
67P Churyumov-Gerasimenko	ESA/Philae	Mottola et al. (2015)	-2.8 ± 0.2	0.05 - 1.10 m	Mantling deposits due to particles falling back to 67P
67P Churyumov-Gerasimenko	ESA/Philae	Mottola et al. (2015)	-3.5 ± 0.3	0.39 - 2.19 m	Lag deposits on 67P

Unlike the Moon and the asteroids, Mars hosted (and in some cases is still hosting) a wealth of processes occurring on its surface, such as aeolian and fluvial, chemical and physical erosion, tectonic events, ancient floods and freeze-thaw fracturing (Bourke et al., 2005; Viles et al., 2005). These phenomena, as well as meteor impacts, may have produced, transported and modified the original boulder size distributions. Hence, even if Mars impact-related SFDs may have been initially comparable to the ones mentioned above, they could have been completely modified throughout the ages.

The first boulder SFDs identified on the Martian surface were derived from Viking lander imaging. By using the NASA/Viking 1 images, Moore and Jakosky (1989) derived a power-law index of -2.66 on rocks ranging between 0.01 and 0.2 m (Table 6). Craddock et al. (1997) suggested that such boulders could mainly be related to impacts, but might also be emplaced by fluvial processes that occurred in the past on Chryse Planitia. In the case of NASA/Viking 2, Moore and Jakosky (1989) derived a similar power-law index on rocks in the size range of 0.01 – 0.4 m, i.e. -2.66 (Table 6), but Thomson and Schultz (2007) suggested a different mechanism than **that thought to have occurred at** Chryse Planitia to explain this size trend, i.e. an impact emplacement origin or impact-derived/impact melt breccias for Utopia Planitia.

Table 6: The SFD derived for Mars boulders and the corresponding size range at which they were derived.

Mars:	Mission	Reference	Power-law index	Diameter size/Range	Notes
Viking Landing site	NASA/Viking 1	Moore and Jakosky (1989)	-2.66	0.2 m	impact related and emplacement by fluvial processes (Craddock et al., 1997 Icarus)
Viking Landing site	NASA/Viking 2	Moore and Jakosky (1989)	-2.66	0.01 - 0.4 m	impact emplaced or impact-derived/impact melt breccias (Thomson and Schultz 2007)
Pathfinder Landing Site	NASA/Pathfinder	Golombek et al. (2003)	Similar to Viking 2	0.05 - 0.4 m	Rocks between 0.5 - 0.8 m have a steeper slope (small angular ejecta versus semi-rounded tabular boulders carried by the flood)

By re-analysing the Viking dataset, Golombek and Rapp (1997) introduced the exponential model to fit the data. The model derived from fracture and fragmentation theory observed on Earth. Their analysis was based on the evidence that power-law curves used in the previous work provided a good fit for diameters greater than about 0.2 m, but not the smaller diameters, which were overestimated by the power-law model. The model introduced by Golombek and Rapp (1997) follows the exponential expression:

$$F(D) = k \exp\{-qD\},$$

where *k* represents the fraction of surface area covered by rocks of all sizes, *q* is the exponent of the fit, *D* is the diameter of the rock and *F(D)* is the cumulative fraction of area covered by rocks with diameter bigger than *D*. In the case of the Viking 1 data the best fitting *k* value

equal to 0.069 was obtained and a *q* value equal to 4.08. In the case of the Viking 2 dataset an *L* value of 0.176 and an *s* value of 2.73 were considered to be excellent fits to the data (Golombek et al., (1997). In the case of the Mars Pathfinder landing site model boulder distributions derived from the Viking exponential fitting curves were used in the range 0.01-1.5 m as well, indicating that the skewed shape of the data is similar to the boulder SFD present at the two Viking landing sites (Golombek et al., 2003). We underline that the presented curves are all related to sizes ranging from centimeters to ~ 1 m.

As usually done in other analysis (e.g. Golombek et al 2008, 2012, Hebrard et al 2012), we compare our results (derived from orbital images) with in-situ analysis (Viking and Pathfinder data). In particular, Fig. 10 shown the cumulative fractional area occupied by boulders ≥ D together with the exponential-law family of curves of boulder coverage derived by Golombek et al 2003.

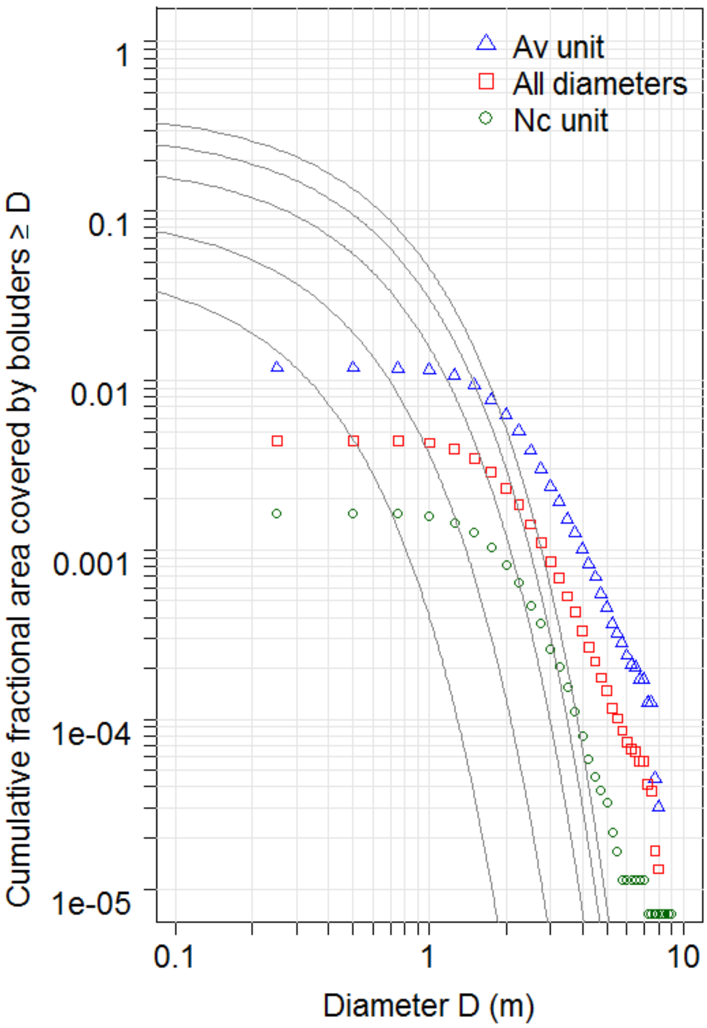

Fig. 10. Cumulative fractional area covered by boulders greater than diameter D versus boulder diameters on the entire Oxia Planum study area and on the Av and Nc units, respectively. The lines are the model distributions as from Golombek et al. (2003) for 5% to 10%, 20%, 30% and 40% boulder coverage.

As expected, Fig 10 shows that the boulder spatial density for the Av unit is much higher than that for the Nc unit (also visible in the HiRISE image, see for instance Figs. 7 and 8). In

particular, the Av unit shows a cumulative fractional area F(D) one-order greater than the Nc unit. By comparing our results with the three curves presented in Fig. 17 of Golombek et al. (2008) and indicated as "few rocks", "moderately rocky" and "very rocky", we conclude that our Nc curve is comparable to the "moderately rocky" one. On the contrary, both the global Oxia Planum curves, as well as the Av curve, are all above the moderately rocky range, with the Av unit showing a trend that is central between the "moderately" and the "very rocky" curves.

As a consequence of the limited resolution of the images, the data flatten considerably at boulder diameters <1.75 m. Fig. 10 also shows differences between the data and the model curves. The same behavior was observed in Heet et al. (2009), that counted rocks on HiRISE images from the Phoenix landing site. Such differences can be due to different processes occurring at the Viking and Mars Pathfinder landing sites (data from which were used to derive the curve represented in Fig. 10) and those processes occurring at Oxia Planum. Another possible explanation, as suggested by Heet et al. (2009), is that a simple exponential-law based on fracture and fragmentation theory used to derive the model curves does not fully explain the boulder populations at the Phoenix landing site. Indeed, this can be true for the proposed Oxia landing site as well, where resurfacing and/or degradation events that occurred on this region, as suggested by Quantin et al., 2016, may have completely changed the original SFDs, hence making the derived curves deviate from the modeled ones.

5.2 Boulder density comparison with other NASA Mars landing sites

To put our boulder densities into context, we collected the available datasets derived from previous NASA Mars landed missions. We are aware that our data were obtained through orbital imaging, but we consider only the boulder densities obtained by lander missions for clast sizes comparable to our case study, i.e. boulders ≥1.75 m.

Golombek and Rapp (1997) analyzed both the Chryse and the Utopia Planitia landing sites of the Viking 1 and 2 missions. By using their exponential SFD, **spatial densities of $3.9\times10^{-9}/m^2$ and $3.4\times10^{-6}/m^2$ for** boulders ≥ 1.75 m are derivable for the Viking 1 and 2 landing areas, respectively. Contrarily, Golombek et al. (2008) presented a much higher **spatial density (close to 1.0×10^{-4} m^{-2}) for boulders ≥ 1.75 m at** the Mars Pathfinder landing site. All three landing sites fall within the rockiest 15% of the planet (Golombek 2003a,b), but **the** Mars Pathfinder landing area is located on a much rougher and rockier surface than either of the Viking landers, i.e. at the outlet of the Ares Vallis on Chryse Planitia.

Despite **the** maximum sizes of 1.5 m **that** are presented, similar boulder **spatial densities to those at** the Viking landing sites have been obtained by the Spirit rover during its traverse **across** Gusev crater (Golombek 2006). For example, the densities performed on the Columbia Memorial Station on Gusev have been shown to be generally lower than those of Viking 1, while they rapidly increase towards the rim of the Bonneville crater, reaching values similar to the Viking 2 landing area.

In the case of the Phoenix lander on Vastitatis Borealis, i.e. the largest lowland region on the northern plains of Mars, Golombek et al. (2012a) derived a density of **boulders ≥ 1.75 m across that is** lower than $1.0\times10^{-6}/m^2$, i.e. **considerably** smaller than the **density at** the Mars Pathfinder landing **site**.

Measurements performed for Gale crater using HiRISE images indicate a spatial density of $5.0\times10^{-5}/m^2$ for boulders **that are** ≥ 1.75 m (Golombek et al., 2012b).

It is evident that the geomorphological settings of the summarized sites are different. Nevertheless, if we compare the Oxia boulder densities with those presented above, it is unambiguous that our study area presents much higher values (i.e. $6.75\times10^{-4}/m^2$). Peak values are obtained for the Av unit (i.e. 1.79×10^{-3}/m^2), whilst the Nc one has a density of 2.55×10^{-4}/m^2: comparable, but still slightly higher, than the Mars Pathfinder landing **site**.

It is true that we do not know how the Oxia boulder size distribution **appears** when sizes smaller than 1.75 m are considered, nor their densities per m^2. Nevertheless, this comparison suggests that a careful evaluation of the risks related to this landing spot, and in particular to the Av unit, has to be taken into consideration **given its moderately to very rocky nature.**

5.3 Boulder production/preservation

A higher value of the power-law index means that i) production rates are different and/or ii) processes decreasing the population **of the larger boulders** and replenishing the smaller size frequencies should have been active.

Martian weathering processes currently **involve** wetting/drying and freeze/thaw cycles, along with thermal shocks due to topographic shading, and they likely act in a similar way **for** any given lithology (Leask and Wilson, 2003). For this reason, the amount of time **over** which alteration processes have occurred becomes the prominent factor. In the Oxia case, the SFD power- and exponential-indices of the Nc unit are steeper than the Av one (Fig. 8), despite its shorter exposure time. For this reason, a different production rate of boulders should be considered for the two separate units.

The two geological units not only show different SFD power-law indices, **but are also characterized by varying boulder spatial density. The** Av unit has a density 7.0 times **larger** than **that of** the Nc (1788 /km^2 versus 255 /km^2 boulders ≥ 1.75 m, respectively). This ratio could be even **larger** if different sectors of Oxia Planum are considered, since **the study area features** ejecta of a 230 m wide crater located near the center of the Nc unit (Fig. 8, black arrows), increasing the local density of boulders (Fig. 7b). The main driver for this difference may **therefore be** the different lithologies where impacts occurred.

When meteor impacts occur, shock waves are generated. These waves are produced when the involved energy is large enough to overcome the threshold between elastic and inelastic behavior of rocks (Jaeger et al., 2007). As mentioned before, the Av unit is **composed of** basaltic lava flows, whereas the Nc one is a clay-rich formation, most likely sedimentary in origin. According to Ahrens and Johnson (1995), shock waves propagate at higher velocities in basalts than in sedimentary rocks. More precisely, velocities are two-to-four times higher in the basaltic case, with greater energy dissipation in the sedimentary lithologies. Moreover, basaltic lava flows and **clay-rich** rocks have different mechanical properties (Chevrier and Mathé, 2007; Hausrath et al., 2008; Yesavage et al., 2015), possibly affecting boulder production/preservation. In particular, igneous rocks have a much higher dynamic strength (three-to-ten times more) than sedimentary ones (Ai and Ahrens, 2004). **This property**, as well as the volatile content of target rocks, **will also** influence melt generation at impact, with less cohesive rocks **producing** increased runout and fluidization of ejecta, instead of production of ballistic projectiles (Osinski et al., 2011). Smaller shock wave velocities and dynamic strengths, as for the sedimentary rocks, suggest the production of a larger number of cracks in sedimentary rocks that would then produce smaller and more abundant boulders. On the contrary, the igneous ones should produce fewer, but larger, blocks. Our SFD results are in good agreement with this theoretical framework, whilst boulder densities are not. However, the much higher exposure age of the Av unit may account for this latter aspect, since it implies a higher number of impacts, producing a larger amount of boulders in all sizes.

Besides the nature of target rocks, detailed studies on terrestrial craters suggest that other factors should be evaluated too. Lonar Crater is a 1.9 km wide impact crater located in Buldhana district, Maharashtra, India. It formed during the Pleistocene Epoch on the Deccan basalt province, one of the largest igneous **provinces** on Earth, **composed** mainly **of** tholeiitic basalts. In the interior walls of the Lonar Crater up to six individual lava flows are exposed (Maloof et al., 2010), thus **making it** a good analog for craters located on our Av unit. Meteor Crater (also known as Barringer Meteorite Crater) is a 1.2 km wide impact crater located in Arizona, USA. This is the result of an iron asteroid impact on layered sedimentary rocks during the Pleistocene Epoch (Kring, 2007), possibly representing a good analog for our Nc unit. The analysis **of** fracture systems **of these two craters highlights the prominent role of pre-impact structures in determining** the stress propagation, crater rim uplift, **final crater** shape, fragmentation and preferential erosion (Kumar and Kring, 2008). Pre-impact conditions such as weathering, layer thickness, and preexisting cracks/fractures are believed to affect also the sizes of boulders constituting the crater's ejecta (Kumar et al., 2014). For the Lonar Crater case, the ejecta are mainly **fine-grained** (i.e. gravel/sand), **nonetheless** boulder clusters have been found in various sectors, with clasts ranging from <1 m to 7.2 m in size. These boulders are partially buried by the ejecta; hence they should be considered as a minimum size term (Kumar et al., 2014). As for the Meteor Crater ejecta, less detailed information is available; however, it is mentioned that the **boulders** in the ejecta range from 0.5 to 30 m in size (Shoemaker, 1987; Ramsey, 2002).

Despite large tectonic **structures are likely** to have affected in a similar way all involved Oxia geological units, this is not the case of intrinsic conditions related to a specific lithology, such as planar bedding of strata or the formation of cooling joints. The calculated SFD **suggests** that no major weakening structures perturbed the lithologies, or that they have been equally affected.

The presented hypotheses need a fundamental validation that can only be accomplished by the future ExoMars rover, which will land on Oxia Planum in 2020. The foreseen panoramic images that will be provided by the Wide Angle Camera of the PanCam instrument (Coates et al., 2015), mounted on the mast of the ExoMars rover, will **provide a** unique opportunity to test our interpretations. Indeed, while travelling towards its multiple targets, the PanCam will provide several views of different terrains and textures, and hence, **will create the opportunity** to perform the SFD computation from boulder sizes ranging from meters to centimeters. This will not only test our analysis, but it will also extend our SFD to the smaller sizes. In addition to the SFD identification, such observations will provide evidence of what kind of processes occurred and/or are possibly still active on the surrounding boulders.

5.4 ExoMars 2020 navigability implications

The ExoMars rover has a mass of 220 kg (56 kg being the payload mass) and a size of 1.2 m x 1.1 m x 2.0 m (http://exploration.esa.int/mars/45084-exomars-rover/), with a ground clearance of 30 cm (see ExoMars 2018 Landing Site Selection User's Manual, Version 1.0, 17 December 2013, hereafter: EXM-SCI-LSS-ESA/IKI-003), i.e. similar to the 29 cm of the Mars Exploration rovers (MER, Leger et al., 2005) and half **that** of the Mars Science Laboratory, MSL (http://mars.nasa.gov/msl/mission/timeline/firstdrive/). This means that every object bigger than 20 cm has to be considered hazardous and **must be** avoided **as indicated in the ExoMars Landing site selection User Manual: http://exploration.esa.int/mars/53458-exomars-2018-landing-site-selection-users-manual/ Reference: EXM-SCI-LSS-ESA/IKI-003. Moreover,** a lateral clearance of about 2-3 m from obstacles is **desirable, given sufficient** operating area. The ExoMars locomotive system is characterised by 6 wheels on a 3-bogie system and each wheel is equipped with 3 actuators: drive, steer and deployment (or wheel walking); this means that contrarily to the MER and MSL, all 6 wheels of the rover can drive and steer simultaneously, providing major manoeuvrability/controllability (Silva et al., 2013). This will mean that **there is the** possibility to steer and drive closer to obstacles than previous missions **have managed,** although only in unavoidable cases.

The ExoMars rover has been planned to achieve two of the most challenging requirements ever tried on the surface of another planet, i.e. the ability to drive an average distance of 70 m per sol (a sol is a Martian day and lasts ~24h37m) and to be able to continue performing its mission without contacting Earth for 2 sols (EXM-SCI-LSS-ESA/IKI-003). It has to be considered that the Martian surface is characterized by several challenges for a rover to drive over, **ranging** from visible obstacles such as rocks, steep slopes (up or down), and craters, to dangerous situations such as slippage. For all these reasons, and in order to **minimize hazards** whilst driving, it **is equipped with** an autonomous navigation system, supported by the combination of the following devices (Silva et al. 2013):

- a sun sensor, that permits an absolute localization on Mars;
- an accelerometer, used to obtain an absolute reference of the rover roll and pitch (or/and tilt angle) by measuring **the Martian** gravity vector;
- a gyroscope, used to propagate the rover attitude;
- panchromatic stereo cameras (at about 2 m above the ground mounted on a pan-tilt assembly) and navigation cameras, in order to provide visual localization of obstacles.

The rover can therefore **be** controlled from Earth with various levels of commanding, executing low-level manoeuvre commands, such as Ackerman curves, point turns, or crabbing, or performing on-board path planning. Nevertheless, greater autonomy will be given to the rover after multiple quantitative evaluations of the terrain type and its characterization, with particular focus on the boulder size-distribution analysis, which is one of the main hazards during navigability.

Our boulder spatial statistics **represent** a reasonable basis to quantify what is the minimum surface percentage that will be unreachable **by** the rover, expressed as a function of the distance from the obstacles. We have considered two representative test case areas, 450m x 400m wide (total area of 1.8×10^5 m^2), in the Nc (center: 24°31'30''W-18°13'56''N) and Av (center: 24°31'28''W-18°15'11''N) units. We have computed seven different distance ranges centered on each boulder ≥1.75 m **across**, from 1 to 20 m, to understand how, and at **what** distances, the rover can travel between two or multiple obstacles.
As it is possible to see from Fig. 11, when the Nc unit is considered, navigable paths can be identified even with a safety distance of 20 m, while there are almost no inaccessible areas at values <10 m. Contrarily, in the case of the Av unit, proper navigable paths have to be carefully studied and identified even at the safety distance of 2-3 m, this becoming particularly rougher if distances > 4 m from the obstacles are considered. **Traveling on the Nc unit will be much easier with respect to the Av one, indeed the cumulative fractional area covered by boulders ≥ diameter D presented in Fig. 10 shows that the Av unit is much rockier than the Nc one. Moreover, the Nc unit has a density of boulders per m^2 which is 7.0 times smaller when compared to the Av unit, leading to a larger autonomy to the rover navigation system. Hence,** the foreseen scientific return of the mission can be greatly enhanced if the Nc unit will be the final landing area of the rover.

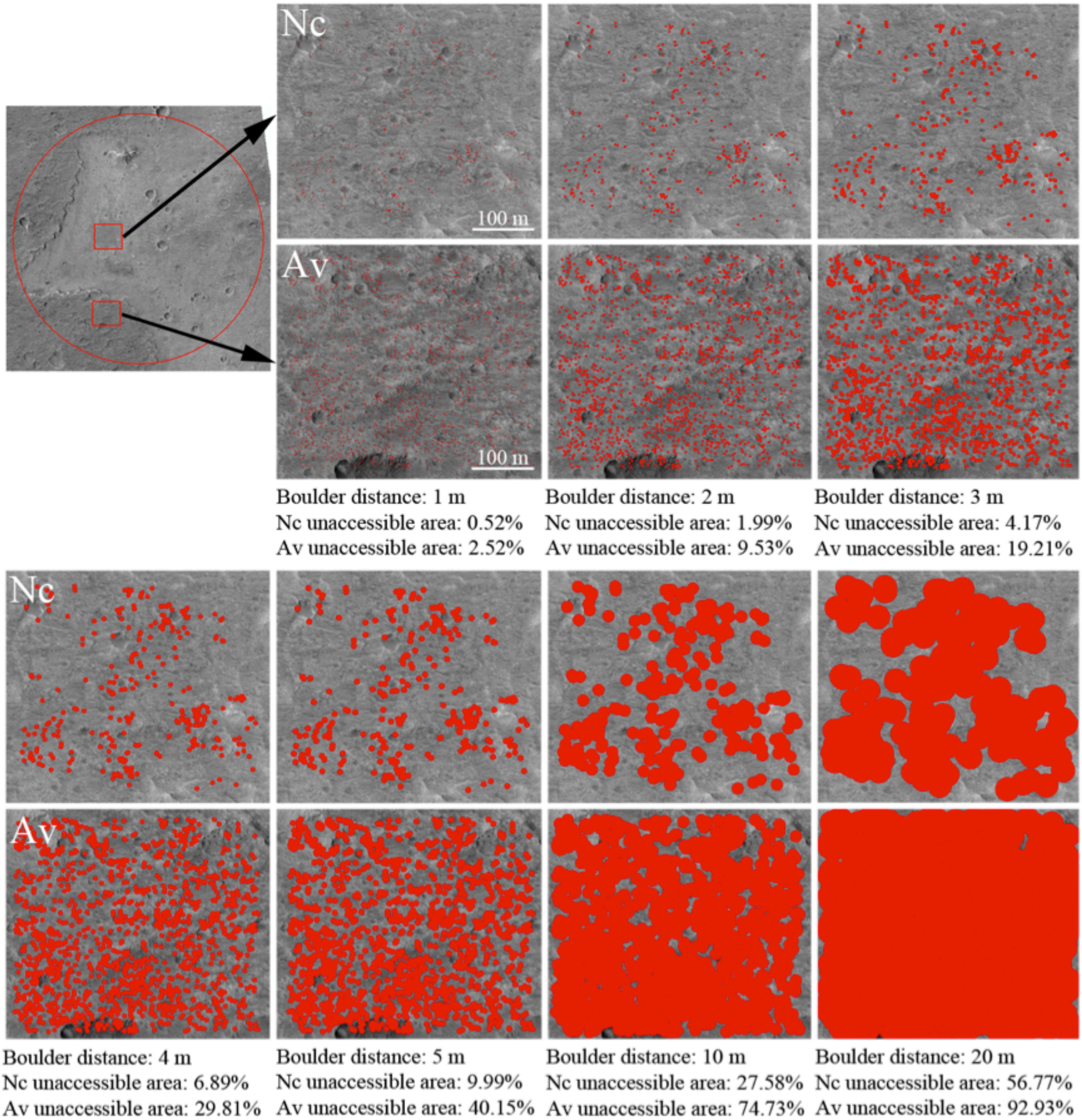

Fig. 11. Upper-left corner: map showing the locations of the two landing test areas in the Nc and in the Av unit. Other images show the buffer distances from the boulders (red areas). The percentages of the areas unreachable by the ExoMars 2020 rover are shown too.

6.0 Summary and Conclusions---

We studied a circular area **of** 12.57 km^2 that is located at the center of the ExoMars Oxia Planum **prime** landing ellipse. Here, both the Noachian clay-rich formation (Nc), as well as the Amazonian volcanic deposit (Av), i.e. the two main units that constitute the entire region, are present.
Using a HiRISE image (0.25 m/pixel), boulders and fine-grained deposits have been mapped. Whilst the former proved to have been properly sampled for sizes bigger than 1.75 m, allowing for additional analysis, the latter appear not to bias the boulder sampling. We derived a global density

of boulders of $6.75\times10^{-4}/m^2$ and size-frequency indices of -4.9 +0.1/-0.2 (power-law fit) and -1.29 +0.04/-0.06 (exponential-law fit) obtained in the range 1.75-6.75 m. When compared to other Mars landing sites observed from orbiters and landers, both the SFD fitting curves and the density of boulders per m^2 indicate that this area is moderately to very rocky (Golombek et al., 2008). Indeed, our study area presents higher values (i.e. $6.75\times10^{-4}/m^2$) than all previous Mars landing sites. Peak values are obtained for the Av unit (i.e. $1.79\times10^{-3}/m^2$), whilst the Nc one has a density of $2.55\times10^{-4}/m^2$, comparable, but still slightly higher, than the Mars Pathfinder landing **site**.

When the Av and the Nc units are considered separately, we identified different SFD power- and exponential-law indices showing a clear higher absolute amount of boulders of all sizes in the Av unit, when compared to the Nc one. This is corroborated by the extremely different density of boulders, that is 7.0 times larger for the Av unit with respect to the Nc one (17.88×10^{-4} versus 2.55×10^{-4} boulders ≥ 1.75 m per m^2). The Av unit deposited above the Nc unit, covering it, therefore a heavier meteoritic occurrence coupled with weathering effects can be invoked to explain this difference. However, these two units are remarkably different in origin, the younger being volcanic (Av) and the older sedimentary (Nc). Specific differences in rock mechanics, such as shock wave velocities and dynamic strengths, suggest the production of a larger number of cracks in sedimentary **rocks, which** would then result in smaller and more abundant boulders. Our SFD results are in good agreement with this theoretical framework, whilst boulder densities are not. However, the much higher exposure age of the Av unit may justify that, **implying** a higher number of impacts, hence a general larger amount of boulders at all sizes.

The discussed hypotheses can only be validated by means of in situ ExoMars observations, which can provide information of different terrains and textures. Indeed, with the ExoMars dataset, the SFD computation of boulder sizes ranging from meters to tens of centimeters will be performed and linked with more precision and detail to the processes that have occurred/are still occurring **on** the Oxia Planum surface.

In addition to the scientific implications **that have been derived** from the presented results, this study provides the quantitative measurements of the **boulder** abundances ≥ 1.75 m **across** for the two geological units identifiable on the future ExoMars 2020 landing site. For this reason, it can be used as a **possible** reference for safety engineering constraints, both during the landing phase and the roving traverse to specific regions of interest. In order to quantify what is the minimum surface percentage that will be unreachable **by** the rover, we have considered two representative test case areas centered in the Nc unit, and in the Av unit, respectively. We have then computed seven different lateral clearance ranges centered on each boulder ≥ 1.75 m, from 1 to 20 m, to understand how and at **what** distances the rover can travel between two or multiple obstacles. **The performed analysis suggests that landing on the Nc unit, rather than on the Av unit, will result in faster and farther navigability of the rover to a specific science target, greatly enhancing the scientific return of the mission.**

Acknowledgements

We thank the three anonymous referees for important and constructive comments and suggestions that lead to a substantial improvement of the paper. **We thank our NASA colleague Dr. Oliver Luke White for thoroughly reviewing the whole document and its English form.** M.P. was supported for this research by an appointment to the NASA Postdoctoral Program at the Ames Research Center, administered by Universities Space Research Association (USRA) through a contract with NASA.

References

Aboudan A., et al., (2014), Automatic rocks detection and classification on high resolution images of planetary surfaces, 45 Lunar and Planetary Science Conference, 2014, 1705.

Ai, H., and T. J. Ahrens (2004). Dynamic tensile strength of terrestrial rocks and application to impact cratering, Meteorit. Planet. Sci., 39, 233–246.

Aldrin, E. E., Armstrong, N. A. and Collins, M. (1969). Apollo 11: Preliminary Science Report, NASA SP-214.

Ahrens, T. J., & Johnson, M. L. (1995). Shock wave data for rocks. Rock Physics & Phase Relations: A Handbook of Physical Constants, 35-44.

Bailen, M. S.; Herkenhoff, K. E.; Howington-Kraus, E. A.; Becker, K.J., 2015. Finding Stereo Pairs With the Pds Planetary Image Locator Tool (Pilot). 46th Lunar Planet. Sci. Conf. 86001, Abstract 1074.

Becker, K.., Archinal, B.., Hare, T.., Kirk, R.., Howington-Kraus, E., Robinson, M.., Rosiek, M.., 2015. Criteria for Automated Identification of Stereo Image Pairs. 46th Lunar Planet. Sci. Conf. 1832, 2703–2704. doi:10.1029/2007JE003000.

Baratti, E., M. Pajola, S. Rossato, C. Mangili, M. Coradini, A. Montanari, and K. McBride (2015), Hydraulic modeling of the tributary and the outlet of a Martian paleolake located in the Memnonia quadrangle, *J. Geophys. Res. Planets, 120,* doi:10.1002/2015JE004812.

Bart, G. D. and Melosh, H. J. (2010). Distributions of boulders ejected from lunar craters, Icarus 209, pp. 337-357.

Bennet, J. G. 1936, Broken Coal, J. Inst. Fuel, 10, 22.

Bourke, M. C., A. J. Brearley, R. Haas, and H. A. Viles (2005). The Surface Features of ‘Pristine’ Flood-transported Boulders. In Mackwell, S. and E. Stansbery (eds.) *Lunar Planet. Sci. Conf. 36th,* p. 2253.

Burrough, P. A., and McDonell, R. A., 1998. Principles of Geographical Information Systems (Oxford University Press, New York), 190 pp.

Carter, J., Loizeau, D., Quantin, C. et al. (2015a). Mineralogic Context of the Circum-Chryse Planitia Candidate Landing Sites for the ExoMars Rover Mission. Geophysical Research Abstracts, 17, EGU2015-5810.

Carter, J., Loizeau, D., Quantin, C. et al. (2015b). Mineralogic Context of the final four, Circum-Chryse candidate landing sites for the ExoMars rover. EPSC Abstracts 10, EPSC2015-661.

Carter, J.; Quantin, C.; Thollot, P.; Loizeau, D.; Ody, A.; Lozach, L., Oxia Planum: A Clay-Laden Landing Site Proposed for the ExoMars Rover Mission: Aqueous Mineralogy and Alteration Scenarios. 47th Lunar and Planetary Science Conference, held March 21-25, 2016 at The Woodlands, Texas. LPI Contribution No. 1903, p.2064

Cheng, Y., A. Johnson, L. Matthies, and A. Wolf (2001), Passive imaging based hazard avoidance for spacecraft safe landing, paper presented at the 9th International Symposium on Artificial

Intelligence, Robotics and Automation for Space (I-SAIRAS), Jet Propul. Lab., Montreal, Quebec, Canada, June.

Chevrier, V., Mathé, P.E., (2007), Mineralogy and evolution of the surface of Mars: A review. Planetary and Space Science, 55 (3), pp. 289-314.

Christensen, P. R. (1986) "The spatial distribution of rocks on Mars" Icarus 68, 217-238, http://dx.doi.org/10.1016/0019-1035(86)90020-5

Ciarletti, V., Hervé, Y., Dorizon, S. et al. (2015). Modelling the performances of the WISDOM radar on the Oxia Planum potential landing site for ExoMars. EPSC Abstracts 10, EPSC2015-574.

Cintala, M. J., McBride, K. M. (1995). Block distributions on the lunar surface: a comparison between measurements obtained from surface and orbital photography. NASA Technical Memorandum 104804. This publication is available from the NASA Center for AeroSpace Information, 800 Ellaidge Landing Road, Linthicum Heights, MD 21090-2934, (301) 621-0390.

Coates, A. J., et al., (2015), PanCam on the ExoMars 2018 Rover: a stereo, multispectral and high resolution camera system to investigate the surface of Mars, 46th Lunar and Planetary Science Conference, held March 16-20, 2015 in The Woodlands, Texas. LPI Contribution No. 1832, p.1812.

Craddock, R. A., et al. 1997, Geology of central Chryse Planitia and the Viking 1 landing site: Implications for the Mars Pathfinder mission, Journal of Geophysical Research, 102, 4161-4183.

Craddock, R. A., M. Golombek, and A. D. Howard (2000) "Analyses of rock size-frequency distributions and morphometry of modified Hawaiian lava flows: Implications for future Martian landing sites" Lunar and Planetary Science XXXI, Abstract #1649, Lunar and Planetary Institute, Houston (CD-ROM).

Curran, D. R., Shockey, D. A., Seaman, L., & Austin, M. 1977, in Impact and Explosion Cratering: Planetary and Terrestrial Implications, eds. D. J. Roddy, R. O. Pepin, & R. B. Merrill, 1057.

Dombard, A. J., Barnouin, O. S., Prockter, L. M., & Thomas, P. C. 2010, Boulders and ponds on the Asteroid 433 Eros, Icarus, 210, 713

Fujiwara, A., Kamimoto, G., & Tsukamoto, A. 1977, Destruction of basaltic bodies by high-velocity impact, Icarus, 31, 277

Garvin, J. B., P. J. Mouginis-Mark and J. W. Head (1981) "Characterization of rock populations on planetary surfaces: Techniques and a preliminary analysis of Mars and Venus" Moon and Planets 24, 355 – 387.

Geissler, P., Petit, J.-M., Durda, D. D., et al. 1996, Erosion and Ejecta Reaccretion on 243 Ida and Its Moon, Icarus, 120, 140.

Golombek, M., and D. Rapp (1997) "Size-frequency distributions of rocks on Mars and Earth analog sites: Implications for future landed missions" Journal of Geophysical Research 102, 4117-4129. http://dx.doi.org/10.1029/96JE03319

Golombek, M. P. et al. (2003a) "Rock size-frequency distributions on Mars and implications for Mars Exploration Rover landing safety and operations" Journal of Geophysical Research 27, 8086 http://dx.doi.org/10.1029/2002JE002035

Golombek, M. P. et al. (2003b) "Selection of the Mars Exploration Rover landing sites" Journal of Geophysical Research 13, 8072 http://dx.doi.org/10.1029/2003JE002074

Golombek, M. P. et al. (2006) "Geology of the Gusev cratered plains from the Spirit rover transverse" Journal of Geophysical Research 111, E02S07 doi:10.1029/2005JE002503.

Golombek, M. P. et al. (2008) "Size-frequency distributions of rocks on the northern plains of Mars with special reference to Phoenix landing surfaces" Journal of Geophysical Research 113, E00A09 http://dx.doi.org/10.1029/2007JE003065

Golombek, M. P, et al., (2012a), Detection and Characterization of rocks and rock size-frequency distributions at the final four mars science laboratory landing sites, Mars, 7, 1-22.

Golombek, M. P, et al., (2012b), Selection of the Mars Science Laboratory Landing Site, Space Sci. Rev, 170, 641-737.

Grant, J. A. et al. (2006) "Distribution of rocks on the Gusev Plains and on Husband Hill, Mars" Geophysical Research Letters 33, L16202 http://dx.doi.org/10.1029/2006GL026964

Hamilton, V. E. and Ruff, S. W. (2012), Distribution and characteristics of Adirondack-class basalt as observed by Mini-TES in Gusev Crater, Mars and its possible volcanic source, Icarus, 218, 917-949.

Hansen, V. L. (2000). Geologic mapping of tectonic planets. Earth and Planetary Science Letters, 176(3–4), 527–542.

Hartmann, W. K. 1969, Terrestrial, Lunar, and Interplanetary Rock Fragmentation, Icarus, 10, 201.

Hausrath, E.M., Navarre-Sitchler, A.K., Sak, P.B., Steefel, C.I., Brantley, S.L., (2008). Basalt weathering rates on Earth and the duration of liquid water on the plains of Gusev Crater, Mars. Geology, 36 (1), pp. 67-70.

Hébrard, E., C. Listowski, P. Coll, B. Marticorena, G. Bergametti, A. Määttänen, F. Montmessin, and F. Forget (2012) "An aerodynamic roughness length map derived from extended Martian rock abundance data" Journal of Geophysical Research 117, E04008 http://dx.doi.org/10.1029/2011JE003942

Heet, T. L. et al. (2009). Geomorphic and geologic settings of the Phoenix Lander mission landing site, Journal of Geophysical Research, E00E04, doi:10.1029/2009JE003416.

Huertas, A., Y. Cheng, and R. Madison (2006), Passive imaging-based multi-cue hazard detection for spacecraft landing, paper presented at the 2006 IEEE Aerospace Conference, Big Sky, Mont., March.

Jaeger, J. C., Cook, N. G. W., Zimmerman, R. W. (2007), Fundamentals of Rock Mechanics – Fourth Edition, Blackwell Publishing, Oxford (475 pp.).

Klacka, J. (1992), Mass distribution in the asteroid belt, Earth, Moon, and Planets (ISSN 0167-9295), vol. 56, no. 1, Jan. 1992, p. 47-52.

Kring, D. A. (2007), Guidebook to the geology of Barringer Meteorite Crater, Arizona (a.k.a

Meteor Crater), LPI Contrib., 1355, 150 pp., Lunar and Planet. Inst., Houston, Texas.

Krishna, N. and Senthil Kumar, P. (2016), Impact spallation processes on the Moon: A case study from the size and shape analysis of ejecta boulders and secondary craters of Censorinus crater, Icarus 264, 274-299.

Kumar, P. and Kring, D. A. (2008), Impact fracturing and structural modification of sedimentary rocks at Meteor Crater, Arizona. Journal of Geophysical Research, Volume 113, Issue E9, CiteID E09009, DOI: 10.1029/2008JE003115

Küppers, M., Moissl, R., Vincent, J.-B., et al. 2012, Boulders on Lutetia, Planet. Space Sci., 66, 71.

Kuiper, G. P. (1965). The Surface Structure of the Moon. In *The Nature of the Lunar Surface,* pp. 99–105. The Johns Hopkins Press, Baltimore.

Le Deit, L., Flahaut, J., Quantin, C., Hauber, E., Mège, D., Bourgeois, O., Gurgurewicz, J., Massé, M., Jaumann, R. (2012). Extensive surface pedogenic alteration of the Martian Noachian crust suggested by plateau phyllosilicates around Valles Marineris, Journal of Geophysical Research E: Planets, 117 (3), art. no. E00J05.

Leask, H. J. and Wilson, L. (2003), Heating and cooling of rocks on Mars: consequences for weathering. 34th Annual Lunar and Planetary Science Conference, March 17-21, 2003, League City, Texas, abstract no.1320

Leger, C. et al. 2005. Mars Exploration Rover surface operations: driving Spirit at Gusev Crater. In IEEE Conference on Systems, Man, and Cybernetics.

Loizeau, D., Flahaut, J., Vago, L.J. et al. (2015a). ExoMars 2018: the four final candidate Landing Sites. Geophysical Research Abstracts, 17, EGU2015-5555-1.

Loizeau, D., Mangold, N., Poulet, F., Bibring, J.-P., Bishop, J.L., Michalski, J., Quantin, C. (2015b). History of the clay-rich unit at Mawrth Vallis, Mars: High-resolution mapping of a candidate landing site. Journal of Geophysical Research E: Planets, 120 (11), pp. 1820-1846.

Malin, M. C., Carr, M. H., Danielson, G. E. et al., Early Views of the Martian Surface from the Mars Orbiter Camera of Mars Global Surveyor (1998), Science, Vol. 279, Iss.5357, p.1681.

Maloof, A.C., Stewart, S.T., Weiss, B.P., Soule, S.A., Swanson-Hysell, N.L., Louzada, K.L., Garrick-Bethell, I., Poussart, P.M. (2010), Geology of Lonar Crater, India. Bulletin of the Geological Society of America, 122 (1-2), pp. 109-126.

Matthies, L., A. Huertas, Y. Cheng, and A. Johnson (2007), Landing hazard detection with stereo vision and shadow analysis, paper presented at the 17th Annual American Astronautical Society Infotech, Rohnert Park, Calif., May.

Mazrouei, S., Daly, M. G., Barnouin, O. S., Ernst, C. M., & DeSouza, I. (2014), Block distributions on Itokawa, Icarus, 229, 181.

McEwen, A. S. et al. (2007) "Mars Reconnaissance Orbiter's High Resolution Imaging Science Experiment (HiRISE)" Journal of Geophysical Research 112, E05S02 http://dx.doi.org/10.1029/2005JE002605

McGetchin, T. R., M. Settle, and J. W. Head (1973), Radial thickness variation in impact crater ejecta: Implications for lunar basin deposits, Earth Planet Sci. Lett., 20, 226–236.

Melosh, H. J. (1984). Impact ejection, spallation, and the origin of meteorites. *Icarus,* 59, pp. 234–260. doi:10.1016/0019-1035(84)90026-5.

Melosh, H. J. (1989), Impact Cratering, 245 pp., Oxford Univ. Press, New York.

Michikami, T., Nakamura, A. M., Hirata, N., et al. (2008), Size-frequency statistics of boulders on global surface of asteroid 25143 Itokawa. *Earth, Planets and Space*, Volume 60, p. 13-20.

Michikami, T., Nakamura, A. M., Hirata, N., et al. (2008), Size-frequency of boulders on global surface of Asteroid 25143 Itokawa, Earth, Planets, and Space, 60, 13.

Moore, H. J. and Jakosky, B. M. 1989, Viking landing sites, remote-sensing observations, and physical properties of Martian surface materials, Icarus, 81, 164-184.

Morris, R. V. et al., (2000), Mineralogy, composition, and alteration of Mars Pathfinder rocks and soils: Evidence from multispectral, elemental, and magnetic data on terrestrial analogue, SNC meteorite, and Pathfinder samples, Journal of Geophysical Research, 105, E1.

Moratto, Z.M., Broxton, M.J., Beyer, R.A., Lundy, M., Husmann, K., (2010), Ames Stereo Pipeline, NASAs Open Source Automated Stereogrammetry Software. In: Proceedings of the 41st Lunar and Planetary Institute Science Conference. Houston, Texas, [2364].

Mottola S., et al., 2015, The structure of the regolith on 67P/Churyumov-Gerasimenko from ROLIS descent imaging, Science, 349, 020232.

Mutch, T. A., Binder, A. B., Huck, F. O., Levinthal, E. C., LIEBES, S., Morris, E. C., ... & Taylor, G. R. (1976a). The Surface of Mars: There View from the Viking 1 Lander. *Science*, *193*(4255), 791-801.

Mutch, T. A., Grenander, S. U., Jones, K. L., Patterson, W., Arvidson, R. E., Guinness, E. A., ... & Wolf, M. R. (1976b). The surface of Mars: The view from the Viking 2 lander. *Science*, *194*(4271), 1277-1283.

Mutch, T. A., Arvidson, R.E., Binder, A.B., Guinness, E.A., Morris, E.C (1977), The Geology of the Viking Lander 2 Site. Journal of Geophysical Research, 82, 28, 4452-4467.

Nyquist, H. (1928), Certain topics in telegraph transmission theory, Trans. Am. Inst. Elect. Eng., 47, 617.

Osinski, G. R., Tornabene, L. L., & Grieve, R. A. (2011). Impact ejecta emplacement on terrestrial planets. *Earth and Planetary Science Letters*, *310*(3), 167-181.

Pajola, M., Vincent, J. B., Guettler, C. et al. (2015), Size-frequency distribution of boulders ≥ 7 m on comet 67P/Churyumov-Gerasimenko, Astronomy and Astrophysics, 583, A37.

Pajola, M., Lucchetti, A., Bertini, I. et al., (2016a), Size-frequency distribution of boulders ≥ 10 m on comet 103P/Hartley 2, Astronomy and Astrophysics, 585, A85.

Pajola, M., Rossato, S., Baratti, E. et al. (2016b), The Simud-Tiu Valles hydrologic system: a multidisciplinary study of a possible site for future Mars on-site exploration, Icarus, 268, 355-381.

Pajola, M., Rossato, S., Carter, J. et al. (2016c), Eridania Basin: an ancient paleolake floor as the next landing site for the Mars 2020 rover, Icarus, 275, 163-182.

Pajola, M., Lucchetti, A., Vincent, J. B. et al., (2016d), The southern hemisphere of 67P/Churyumov-Gerasimenko: Analysis of the preperihelion size-frequency distribution of boulders ≥ 7 m, Astronomy and Astrophysics, 592, L2.

Pajola, M., Oklay, N., La Forgia, F. et al., (2016e), Aswan site on comet 67P/Churyumov-Gerasimenko: Morphology, boulder evolution, and spectrophotometry, Astronomy and Astrophysics, 592, A69.

Pajola, M., Mottola, S., Hamm, M. et al., (2016f), The Agilkia boulders/pebbles size-frequency distributions: OSIRIS and ROLIS joint observations of 67P surface. MNRAS, 462, issue Suppl 1, pp. S242-S252.

Pajola M., Höfner S., Vincent, J. B. et al., (2017), The pristine interior of comet 67P revealed by the combined Aswan outburst and cliff collapse. Nature Astronomy, 1, 92.

Quantin, C., Carter, J., Thollot, P. et al. (2015), Oxia Planum: a suitable landing site for ExoMars 2018 Rover, European Planetary Science Congress 2015, held 27 September - 2 October, 2015 in Nantes, France, id.EPSC2015-704.

Quantin, C., Carter, J., Thollot, P. et al. (2016). Oxia Planum, the landing site for ExoMars 2018, 47th Lunar and Planetary Science Conference 2016.

Ramsey, M. S., (2002) Ejecta distribution patterns at Meteor Crater, Arizona: On the applicability of lithologic end-member deconvolution for spaceborne thermal infrared data of Earth and Mars, J. Geophys. Res., 107(E8).

Reach, W. T., Vaubaillon, J., Kelley, M. S., Lisse, C. M., & Sykes, M. V. 2009, Distribution and properties of fragments and debris from the split Comet 73P/Schwassmann-Wachmann 3 as revealed by Spitzer Space Telescope, Icarus, 203, 571.

Sammis, C. G. & Biegel, R. L. (1989). Fractals, fault-gouge, and friction, *Pure Appl. Geophys.* 131,255-27 1.

Senthil Kumar, P., K. J. Prasanna Lakshmi, N. Krishna, R. Menon, U. Sruthi, V. Keerthi, A. Senthil Kumar, D. Mysaiah, T. Seshunarayana, and M. K. Sen (2014). Impact fragmentation of Lonar Crater, India: Implications for impact cratering processes in basalt, *J. Geophys. Res. Planets*, 119, 2029–2059, doi:10.1002/2013JE004543.

Shoemaker, E. M. (1965). Preliminary Analysis of the Fine Structure of the Lunar Surface in Mare Cognitum. In Hess, W. N., D. H. Menzel, and J. A. O'Keefe (eds.) *The Nature of the Lunar Surface,* pp. 23–77. The Johns Hopkins Press, Baltimore.

Shoemaker, E. M. et al. (1970). Apollo 12: Preliminary Science Report, NASA SP-235.

Shoemaker, E. M. and E. C. Morris (1970). Geology: Physics of fragmental debris. *Icarus,* 12, pp. 188–212. doi:10.1016/0019-1035(70)90072-2.

Shoemaker, E.M. (1987), Meteor Crater, Arizona, Geological Society of America Centennial Field Guide - Rocky Mountain Section.
Schoutens, J. E. 1979. Nuclear Geoplosics Sourcebook, Volume IV, Part II- Empirical Analysis of Nuclear and High-Explosive Cratering and Ejecta, Defense Nuclear Agency DNA 6501H-4-2.

N. Silva, R. Lancaster, and J. Clemmet 2013, ExoMars Rover Vehicle Mobility Functional Architecture and Key Design Drivers, 12th Symp. on Advanced Space Technologies in Robotics and Automation (ASTRA), Noordwijk, The Netherlands, May 2013.

Surveyor Scientific Evaluation and Analysis Team (1966a). Size Distribution of Debris on the Lunar Surface and the Characteristics of the Fine Matrix. In Lunar and Plane- tary Programs Division, Office of Space Science and Applications (ed.) *Surveyor 1: A Preliminary Report,* pp. 31–32. NASA SP-126.

Smith, D. E., et al. (2001), Mars Orbiter Laser Altimeter: Experiment summary after the first year of global mapping of Mars, J. Geophys. Res., 106(E10), 23689–23722.

Squyres, S. W., et al., (2006), Overview of the Opportunity Mars Exploration Rover Mission to Meridiani Planum: Eagle Crater to Purgatory Ripple, Journal of Geophysical Research, Volume 111, Issue E12, CiteID E12S12.

Stolper, E. M., et al., (2013), The Petrochemistry of Jake_M: A Martian Mugearite, Science, 341, no.6153.

Thomas, P. C., Veverka, J., Robinson, M. S., and Murchie, S. 2001, Shoemaker crater as the source of most ejecta blocks on the asteroid 433 Eros, Nature, 413, 394.
Thomson, B. J., and Schults, P. H. 2007, The geology of the Viking lander 2 site revisited, Icarus, 191, 505-523.

Torson, J.M., and Becker, K.J. (1997) ISIS - A Software Architecture for Processing Planetary Images, 1036 Lunar Planet. Sci. XXVIII, Houston, Texas, Abstract [1219].
Turcotte, D. L. 1997, Fractals and Chaos in Geology and Geophysics (CUP)

Ward, J. G. et al. (2005) "The size-frequency and areal distribution of rock clasts at the Spirit landing site, Gusev Crater, Mars" Geophysical Research Letters 32, L11203 http://dx.doi.org/10.1029/2005GL022705

Yesavage, T., Thompson, A., Hausrath, E.M., Brantley, S.L., (2015). Basalt weathering in an Arctic Mars-analog site. Icarus, 254, pp. 219-232.

Yingst, R. A., A. F. C. Haldemann, K. L. Biedermann and A. M. Monhead (2007) "Quantitative morphology of rocks at the Mars Pathfinder landing site" Journal of Geophysical Research 112, E06002 http://dx.doi.org/10.1029/2005JE002582

Yingst, R. A., L. Crumpler, W. H. Farrand, R. Li and P. de Souza (2010) “Constraints on the geologic history of ‘Home Plate’ materials provided by clast morphology and texture” Journal of Geophysical Research 115, E00F13 http://dx.doi.org/10.1029/2010JE003668

Viles, H. A., A. J. Brearley, M. C. Bourke, and J. Holmlund (2005). What Processes Have Shaped Basalt Boulders on Earth and Mars? Studies of Feature Persistence Using Facet Mapping and Fractal Analysis. In Mackwell, S. and E. Stansbery (eds.) *Lunar Planet. Sci. Conf. 36th,* p. 2237.

Wentworth C. K., (1922). A Scale of grade and class terms for clastic sediments. J. Geol., 30, 377, pp.377-392.

Wu, Q., Borkovee, M. & Sticher, H. (1993). On particle-size distributions in soils, *Soil Sci. Soc. Am. J.* 57,883-90.